Nanoscale Horizons

Accepted Manuscript

ROYAL SOCIETY OF CHEMISTRY

rsc.li/nanoscale-horizons

Journal Name

REVIEW

Electrode materials with tailored facets for electrochemical energy storage

Received 00th January 20xx,
Accepted 00th January 20xx

DOI: 10.1039/x0xx00000x

www.rsc.org/

Faxing Wang,[a,b] Xiaowei Wang,[b] Zheng Chang,[b] Yusong Zhu*,[a] Lijun Fu*, [a] Xiang Liu [a] and Yuping Wu*[a,b]

In recent years, the design and morphological control of crystals with tailored facets are becoming a hot spot. For electrode materials, morphologies play important roles in their activities because their shapes determine that how many facets of specific orientation are exposed and therefore available for surface reactions. This review focuses on the strategies in crystal facets control and the unusual electrochemical properties of electrode materials bounded by tailored facets. Electrode materials with tailored facets, here, include transition metal oxides such as SnO_2,Co_3O_4, NiO, Cu_2O, and MnO_2, elementary substances such as Si and Au, and intercalation compounds like $Li_4Ti_5O_{12}$, $LiCoO_2$, $LiMn_2O_4$, $LiFePO_4$, and $Na_{0.7}MnO_2$ for various applications of Li-ion battery, aqueous rechargeable lithium battery, Na-ion battery, Li-O_2 battery and supercapacitor. How these electrode materials with tailored facets affect their electrochemical properties are discussed. Finally, research opportunities as well as the challenges for this emerging research frontier are highlighted.

1. Introduction

The specific exposed facets and their related surface energies exert significant influences on the kinetics and thermodynamics of heterogeneous reactions occurring at the interface.[1-3] Thus, the design and morphological control of crystals with tailored facets is becoming a hot spot in scientific research.[4-9] In the case of anatase TiO_2, for example, it is usually exposed with low index facets such as (001) and (101) as shown in **Fig.1**. Specifically, its most common crystal shape is the truncated octahedral bipyramid comprising eight (101) facets (94%) on the sides and two (001) facets (6%) on the top and bottom truncation facets.[5] However, theoretical studies indicate that the (001) facets of anatase TiO_2 is much more reactive than its other surfaces. [9] The surface energy is closely related to the density of undercoordinated Ti atoms. The right panel in **Fig. 1** summarizes the possible shapes that may be produced. Synthesis of high energy facets of TiO_2 has been achieved to improve its properties and extend its applications in the past decades.

At the same time, rechargeable batteries and supercapacitors are emerging as two important classes of electrochemical energy storage devices.[10,11] Electrochemical energy storage involves physical interaction and/or chemical reaction at the surface or interface. The discharge/charge processes in rechargeable batteries and supercapacitors are accompanied by the transport of active ions across the surface of crystals. Thus, the interaction between active ions in electrolyte and surface of crystals is essential in the field of batteries and supercapacitors. To develop electrode materials with specific facets is of vital significance to control interaction between active ions and surfaces of crystals. Different facets with different surface atomic structures may exhibit distinct abilities in hosting guest materials. In this regard, electrode materials with preferred orientation and exposure of facets have received widespread attention for electrochemical energy storage in the recent years. For examples, our group reported the synthesis of $LiMn_2O_4$ nanotubes with exposed (400) plane,[12] $LiFePO_4$ nanoparticles with major exposure of (010) plane,[13,14] and hollow Li_3VO_4 microbox with exposed (200) plane.[15,16] Interestingly, based on density function theory calculations and in situ mass measurement (electrochemical quartz crystal microbalance), we found that when the $LiFePO_4$ (010) surface is contacted with aqueous solution, there is always a water molecule chemisorbed near the Fe site on the surface. This water molecule strengthens the Li binding on surface sites and increases the binding energy, which lowers the energy barrier for Li diffusion from the subsurface to (010) surface.[13]

However, most reviews on the unusual properties of crystals exposed by highly reactive facets mainly focus on the field of catalytic studies and gas adsorption.[4-6] Those catalytic or adsorption processes critically depend on the surface atoms' arrangement and the number of dangling bonds on different crystal planes. Even though there are a few reviews dealing with crystals with tailored facets for electrochemical energy storage, they usually only mainly focus on one specific electrode materials such as TiO_2, [4,17,18] Co_3O_4, [19] and positive electrode materials [20] with predominantly exposed facets. Therefore, a comprehensive summary of crystals with tailored facets for electrochemical energy storage is lacking and highly desirable in order to rationally promote the further development of rechargeable batteries and supercapacitors.

[a] College of Energy and Institute for Electrochemical Energy Storage, Nanjing Tech University, Jiangsu Province , Nanjing 211816, China, E-mail: zhuys@njtech.edu.cn (Zhu); l.fu@njtech.edu.cn (Fu); wuyp@fudan.edu.cn (Wu).
[b] New Energy and Materials Laboratory (NEML), Department of Chemistry, Fudan University, Shanghai 200433 , China

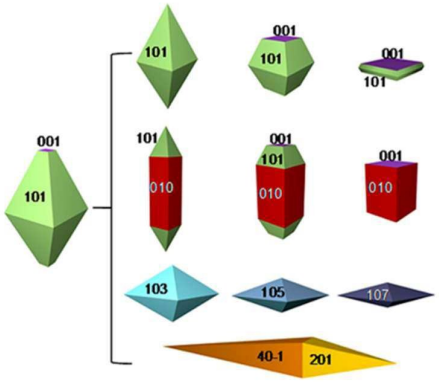

Fig. 1 Equilibrium crystal shape of anatase TiO_2 through the Wulff construction and the evolved other shapes (modified from ref. 5, copyright permission from American Chemical Society).

In this review, we will summarize the latest developments regarding applications of electrode materials with tailored facets for electrochemical energy storage in the five fields, namely, Li-ion battery, aqueous rechargeable lithium battery, Na-ion battery, Li-O_2 battery and supercapacitor. It will be shown that there is some relationship between crystal with exposed facets and unusual electrochemical properties. A particular focus is directed to strategies in their shape control and the uniqueness of electrode materials with preferred orientation and facets in energy storage applications. To facilitate further research and development in this promising field, some future trends or directions are also discussed.

2. Electrode materials with tailored facets for Li ion battery

Lithium is the third lightest element and has the lowest redox potential of all known elements (-3.05 V vs. the standard hydrogen potential). Though lithium has been incorporated into battery systems since the late 1960s, rechargeable lithium ion batteries were commercialized by Sony Corporation in 1991.[21,22] A Li-ion battery consists of three functional components (the negative electrode, positive electrode and electrolyte), and functions by converting a chemical potential into electrical energy via Faradaic reactions. This process includes heterogeneous charge transfer occurring at the surface of an electrode. Therefore, the crystal structure and morphology are critical to the reaction rate and transfer processes.[23,24]

2. 1 Negative electrode materials with tailored facets

Researches on negative electrode materials for Li-ion battery can be developed on the three different categories, which are basically identical to those: (1) intercalation compounds such as TiO_2, $Li_4Ti_5O_{12}$ and Li_3VO_4; (2) elementary substances based on alloy reaction such as Si, Sn and Ge; and (3) metal oxides with conversion reaction such as NiO, Co_3O_4 and Fe_2O_3. Some characteristics of them are summarized in **Table 1**.

Table 1 Some negative materials with tailored facets and their primary characteristics.

Electrode	Tailored facets	Preparation method	Specific capacity / mAh g^{-1}	Rate /A g^{-1}	Cycle	Ref
TiO_2	(001)	Solvothermal method	200	3.4	100	25
$Li_4Ti_5O_{12}$	(011)	Hydrothermal + calcination	205	4	100	26
SnO_2	(110)	Precipitation +calcination	918	5	50	27
NiO	(110)	Hydrothermal + calcination	700	40C	1000	28
Cu_2O	(001)	Hydrothermal method	841	6.7	1000	29
Co_3O_4	(110)	Hydrothermal method	946	2	50	30

2.1.1 TiO_2 with tailored facets

As one of the most promising negative electrode candidates for Li ion batteries, TiO_2 exhibits excellent chemical stability, non-toxicity, low cost, low volume expansion as well as the advantages of high operation safety with an operating voltage higher than 1 V above the potential where most types of electrolytes or solvents are reduced.[31-33]

Several years ago, anatase single crystal TiO_2 with 47% of the highly reactive (001) facets was prepared by using hydrofluoric acid (HF) as a capping agent under hydrothermal conditions.[1] The choice of capping agents is essential in controlling the facets grown in the TiO_2 crystals. The adsorption of the capping agents reduces the surface free energy of materials with more active sites inhibiting the crystal growth along the corresponding direction. This breakthrough has attracted great interests in various synthesis methods to achieve TiO_2 with specific facets, including hydrothermal,[34-36] solvothermal,[25,37,38] and template methods. [39]

For anatase TiO_2, the Li^+ ion diffusion coefficient is approximately 2.0×10^{-13} cm^2 s^{-1} along the [001] orientation while it is only 7×10^{-14} cm^2 s^{-1} in the [101] orientation.[40] The energy barriers calculated based on density functional theory for Li^+ ion insertion into (001) and (101) surfaces are 1.33 and 2.73 eV, respectively. [41] Thus, the charge transfer and chemical diffusion coefficient for TiO_2 is greatest along the (001) facet, and exposing these facets can result in a lower energy barrier for faster and more Li^+ ion intercalation. As shown in **Fig. 2**, anatase TiO_2 nanosheet composed of 80% exposed (001) facets demonstrates high-rate insertion/extraction of Li ions over extended cycling compared to anatase TiO_2 with dominant (101) facets. These two samples have very different percentages of exposed (001) facets, about 80% for the nanosheets (**Fig. 2a**) and only about 2.2% for the octahedral sample dominated by (101) facets (**Fig. 2b**). At 10C, anatase TiO_2 nanosheets with 80% (001) surface show a higher specific capacity compared to (101) dominated anatase TiO_2 nano-octahedra (**Fig. 2c**). More Li^+ ion

insertion/extraction can occur through the less thermodynamically favored (001) surface, which agrees well with theoretical prediction of a lower barrier for surface transmission of Li^+ ions across this facet compared with the (101) surface.

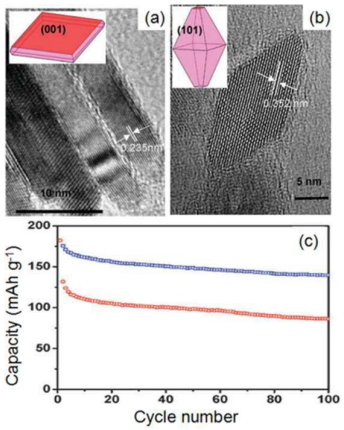

Fig. 2 TEM micrographs of the anatase TiO_2 with dominant (a) (001) and (b) (101) surface (Insets are corresponding geometrical models of the anatase single crystals), and (c) The cycling behaviors with dominant (001) (upper) and (101) (lower) facets at 10C (modified from ref. 41, copyright permission from The Royal Society of Chemistry).

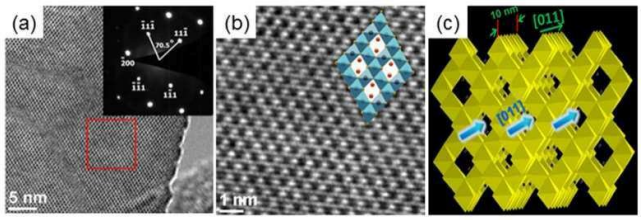

Fig.3 (a) The top viewed HRTEM micrographs of the nanoflake (inset is the corresponding SAED pattern); (b) partial enlarged details of the red box part in (a). The inset in b shows the corresponding crystal structure of spinel $Li_4Ti_5O_{12}$ in projection along (011); and (c) schematic illustration of Li^+ ions diffusion in spinel structured $Li_4Ti_5O_{12}$ (modified from ref. 26, copyright permission from American Chemical Society).

Ultrathin anatase TiO_2 nanosheets with nearly 100% exposed (001)) facets was also synthesized.[25] The individual nanosheet adopts a random orientation and forms a three-dimensional highly nanoporous structure with a high specific surface area (170 m^2 g^{-1}). The short diffusion path length in this ultrathin TiO_2 nanosheets leads to highly efficient solid-state diffusion of Li^+ ions. So, even at a high current rate of 20 C (3.4 A g^{-1}), a reversible capacity of 95 mA h g^{-1} could still be delivered. Similar results have also been demonstrated by sandwich-like TiO_2/C composite hollow spheres [34] and TiO_2/graphene aerogels composites.[35] Apart from the reactive (001) surface, the strong connection between TiO_2 and conductive carbon also improve the electron transport efficiency. All these results clearly demonstrate the significance of tailoring the facets of TiO_2 crystals in improving the lithium storage capability as negative electrode materials.

2.1.2 $Li_4Ti_5O_{12}$ with tailored facets

Spinel $Li_4Ti_5O_{12}$ is regarded as another ideal negative electrode material with long cycling stability due to zero volume change when Li ions intercalate into and de-intercalate out.[42] $Li_4Ti_5O_{12}$ can accommodate three Li ions with a theoretical specific capacity of 175 mAh g^{-1} at relatively higher operating potential of 1.55 V (vs. Li^+/Li), corresponding to a chemical formula of $Li_7Ti_5O_{12}$.[43] However, its rate capability is relatively low because of a large polarization at high charge/discharge rates resulting from the poor electrical conductivity and sluggish Li ion diffusion.

Spinel $Li_4Ti_5O_{12}$ has plenty of porous channels along the [011] direction. These porous channels are favorable for fast Li ion diffusion. Therefore, spinel $Li_4Ti_5O_{12}$ negative electrode with preferentially exposed (011) plane should bring benefit to high electrochemical performance due to the directly accessible channels for the intercalation of Li ions. With this consideration in mind, $Li_4Ti_5O_{12}$ hollow spheres composed of nanoflakes with preferentially exposed (011) facets were fabricated via a facile hydrothermal processing and following calcination.[26] **Fig. 3** shows the top viewed HRTEM micrographs of the $Li_4Ti_5O_{12}$ nanoflake. Two sets of lattices form a dihedral angel of approximately 70.5° to each other with an equal inter-fringe spacing of 0.49 nm, corresponding to its (111) planes (**Fig. 3a**). The corresponding SAED pattern of the same region can be indexed to diffraction spots of the (011) zone, indicating that nearly 100% exposed surfaces are (011) planes. More detailed crystal structure of the spinel $Li_4Ti_5O_{12}$ in projection along (011) can be found in partial enlarged HRTEM micrographs (**Fig. 3b**).

Cycled at a high current density of 4 A g^{-1}, the nanoflake shows a high discharge capacity of 148 mAh g^{-1} in the first cycle, giving a retention rate of approximately 74% after 100 cycles.[26] The preferentially exposed (011) planes in the $Li_4Ti_5O_{12}$ nanoflakes provide directly accessible channels for the intercalation/deintercalation of Li ions along the (011) direction (**Fig. 3c**). Besides, the $Li_4Ti_5O_{12}$ nanoflake, with a thickness of approximately 10 nm, significantly decreases the diffusion distance for Li ions compared with the bulk materials. Additionally, the hollow structure of the $Li_4Ti_5O_{12}$ spheres facilitates the permeation of electrolyte within the electrode.

2.1.3 Si with tailored facets

Silicon (Si) as the negative electrode for Li ion battery has a high theoretical capacity of 4200 mAh g^{-1} when $Li_{4.4}Si$ is formed, which is more than 10 times that of commercial graphite. Its discharging potential, about 0.2 V (vs. Li^+/Li), is lower than most of other alloy-type and metal oxide negative electrode materials.[44] Such a low operation potential can lead to a high energy density of full cells. Besides, Si is environmentally friendly and abundant in the Earth crust. However, Si exhibits significant volume changes (>400%) during Li alloying and dealloying. These changes cause cracking and crumbling of the electrode material and a consequent loss of electrical contact between individual particles and hence severe capacity fading.[45,46]

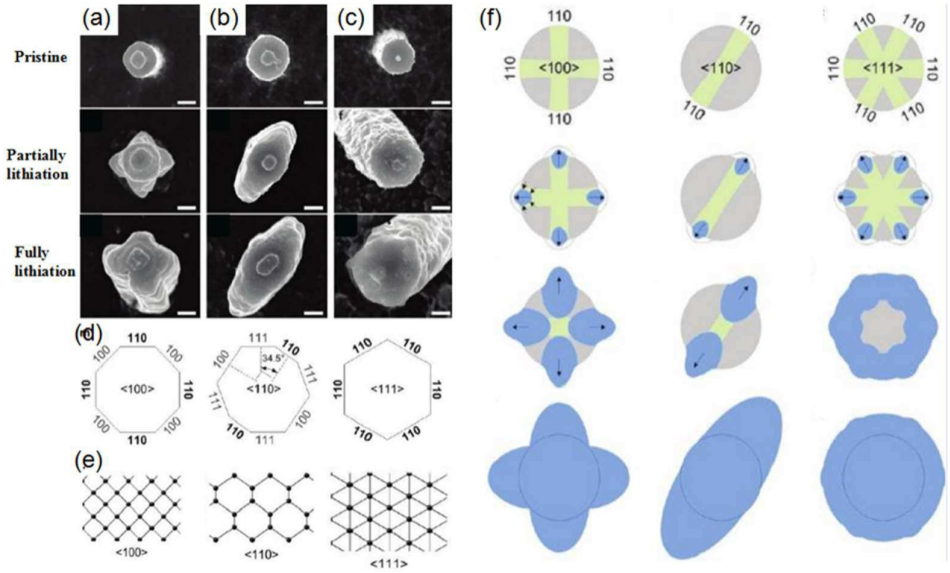

Fig. 4 Top-viewed SEM micrographs of Si nanopillars with crystal orientation along (a) (100), (b) (110), and (c) (111) planes upon lithiation and each lithiation state, (d) schematic diagram of the crystallographic orientation of the facets on the sidewalls of each of the pillars, (e) view along three different directions of the diamond cubic lattice, and (f) schematic explaining anisotropic expansion of Si nanopillars (modified from ref. 48, copyright permission from American Chemical Society).

The intercalation of a Li atom into the surface and subsurface layers of Si (100) and Si (111) planes was studied by density functional calculation.[47] It is found that once the Li atom is incorporated into the Si surface, Li diffuses faster by at least two orders of magnitude along the [100] direction than along the [111] direction. Similar result was also obtained through experimental studying the shape and volume changes of Si with different orientations upon first lithiation.[48] The Si nanopillars with axial orientations along (100), (110) and (111) planes were fabricated by etching a Si wafer surface with SiO_2 nanospheres as etch mask.

The nanopillars stand vertically on a fixed substrate as shown in **Fig. 4**. When they were discharged to 0.12 V (vs. Li^+/Li) (partially lithiation), all of them show obvious anisotropic cross-sectional expansion. As shown in **Fig. 4(a)-(f)**, the initially circular (100), (110), and (111) pillars transfer to a cross, an ellipse, and a hexagon, respectively. With further discharged to 0.01 V (vs. Li^+/Li) (full lithiation), the cross and elliptical cross-sectional shapes of the (100) and (110) nanopillars become more significant and the cross section of the <111> nanopillar is slightly hexagonal. In all three cases, the nanopillars expand most significantly along the (110) family of directions (**Fig. 4d**) because this channel is much larger than those along the (100) and (111) directions (**Fig. 4e**). Besides, the (111) and (100) nanopillars shrink in height after partial lithiation, while (110) nanopillars increase in height. It was suggested that Li enters the crystalline Si nanostructure through <110> ion channels and induces the collapse of some (111) facets by breaking Si-Si bonds. These findings provide a guide for developing high power Si electrode by increasing the prevalence of (110) facets to promote fast diffusion of Li ions. However, unfortunately few efforts have been put into the development of Si with tailored (110) facets.

2.1.4 SnO_2 with tailored facets

SnO_2 is one of another most extensively studied negative electrode materials because of its abundance, safe lithiation potential and high theoretical capacity (782 mAh g^{-1}). [49,50] SnO_2 reacts with lithium in a two-step process ($SnO_2 + 4Li^+ + 4e^- \rightarrow Sn + 2Li_2O$ and $Sn + xLi^+ + xe^- \leftrightarrow Li_xSn$). Similar to Si, the practical application of SnO_2 typically suffers from a large volume expansion (up to 250%) and agglomeration during the Li-alloying/dealloying process, resulting in pulverization of the electrode and rapid capacity fading.

Ultrathin SnO_2 nanosheets along the [110] direction were assembled by oriented attachment of SnO_2 nanoparticles with the help of additives (ethanol, $NH_3 \cdot H_2O$ and urea).[51] The -OH group of ethanol, $-NH_2$ group of urea, and NH_4^+ of aqueous ammonia play important roles as surface-modifying reagent in the reactions. These functional groups can lead to the variation in surface energy of SnO_2 nanocrystals due to their different abilities to bind Sn ions or form hydrogen bonds. In another report, N-doped graphene-SnO_2 sandwich films were fabricated via a three-step route.[27] First, 7,7,8,8-tetracyanoquinodimethane anion ($TCNQ^-$) was absorbed on the surface of graphene under the electrostatic repellency preventing the inter- or intra- $\pi-\pi$ stacking of graphene. After addition of the Sn (II) salt, the graphene layers containing Sn-TCNQ self-assembled into a sandwich because of the strong electrostatic interactions between Sn^{2+} and $TCNQ^-$. After that, the obtained precipitation was dried and annealed under inert gas atmosphere to obtain the sandwich-type graphene-SnO_2. During the synthesis process, the interlayer space of graphene acting as a nanoscale reactor effectively restricts the growth of the SnO_2 nanoparticles and further drives the fusion of two or more nanoparticles into a 1D nanostructure within the lamellar

superstructure. Most particles are epitaxially fused together towards [110] because of the continuity of the lattice (110) planes across the interface, suggesting that the oriented attachments occur along the (110) facets.

A much higher reversible capacity of 534 mAh g^{-1} was achieved for highly oriented SnO_2 nanosheets along the (110) direction even after 50 cycles.[27] The SnO_2 nanosheets shows a greatly enhanced lithium storage capability compared to commercial SnO_2 nanoparticles. The specific capacity is maintained as high as 683 and 619 mAh g^{-1} at 1 and 2 A g^{-1}, respectively. Even at a current density of 5 A g^{-1}, it still delivers a capacity of 504 mAh g^{-1}. As for the commercial SnO_2 nanoparticles, the capacity rapidly decays to 153 mAh g^{-1} at 1 A g^{-1}, and to 12 mAh g^{-1} at 2 A g^{-1}. In the sandwich structure, the electronic transport length in the graphene-SnO_2 is effectively shortened to a level comparable to the particle size of the nanocrystals. Moreover, the ultra-small SnO_2 nanocrystals (2 – 5 nm) with preferred orientation (110) planes render a very short transport length for Li ions during insertion/extraction process.

2.1.5 Transition metal oxides based on a conversion reaction mechanism with tailored facets

A series of transition metal oxides has received growing interests as potential negative electrode materials for next-generation Li ion battery. The lithium storage mechanism of these transition metal oxides is based on the redox conversion reaction, where the metal oxides are reduced to related metallic nanoclusters dispersed in Li_2O matrix upon lithiation and are then reversibly restored to their initial oxidation states during delithiation. These transition metal oxides usually suffer from poor cyclability associated with the large volume change during charge/discharge process. And the low conductivity induces bad rate behavior.

The properties of transition metal oxides crystals are largely determined by exposed external surfaces. NiO crystals with dominantly exposed (110) reactive facets were obtained by a thermal conversion of hexagonal $Ni(OH)_2$ nanoplatelets.[28] The prepared NiO crystals preserve the single crystalline feature and hexagonal shape of the precursor $Ni(OH)_2$ nanoplatelets. This may be due that those (111) crystal facets of $Ni(OH)_2$ and NiO (110) crystal facets have low crystal mismatch. The (110) lattice plane of $Ni(OH)_2$ crystals has a d-spacing of 0.29 nm, which is very close to that of the (111) plane of NiO crystals (0.24 nm). The control of the crystal mismatch within a low range is highly favorable for monocrystallization.

CuO nanoplatelets with exposed (001) facets and hollow hierarchical Fe_2O_3 spheres self-organized from the ultrathin nanosheets of Fe_2O_3 were prepared by hydrothermal process.[29, 52] The ultrathin Fe_2O_3 nanosheet subunits possess an average thickness of around 3.5 nm and show preferential exposure of (110) facets. The highly exposed (110) facets of Fe_2O_3 are largely dominated by the high density of Fe atoms. The role of crystal facet engineering in the formation of Fe_2O_3 mesocrystals was also studied in rhombic hematite mesocrystal by the time-resolved fusion in solvothermal approach using N,N-dimethylformamide (DMF) and methanol as the mixed solvent.[53] The reactants chemically transform into active particles to form the hematite crystals as the following formulae shown:

$$HCON(CH_3)_2 + H_2O \rightarrow NH(CH_3)_2 + HCOOH \quad (1)$$

$$HCOOH + CH_3OH \rightarrow HCOOCH_3 + H_2O \quad (2)$$

$$2Fe^{3+} + 3H_2O + 6NH(CH_3)_2 \rightarrow Fe_2O_3 + 6NH_2(CH_3)_2^+ \quad (3)$$

The Fe_2O_3 particle units with a common crystallographic orientation sharing (012) facets are attributed to that the cationic thermal DMF hydrolysis product can adsorb the O-terminated layer of (012) facets, which could stabilize the high-energy (012) facets. Then, crystallographic fusion happens because high interface energy leads to high colloidal attraction, where bonding between the particles allows the system to gain a substantial amount of energy by eliminating two high-energy surfaces. In this case, the exposed facet can be easily tuned by controlling the composition of the mixed solvent. Increasing the amount of CH_3OH can accelerate Fe^{3+} ions hydrolysis by the esterification reaction (Eqn 2); while decreasing the amount of DMF results to less $NH_2(CH_3)^{2+}$ to protect primary particles with exposed high-energy (012) facets, leading to the formation of the particles with low-energy facets. So the fusion process can be hindered since the attraction between low-energy facets cannot provide sufficient energy.

The shape control of Co_3O_4 with different well-defined crystal plane structures was facilely achieved by simply changing the content of NaOH and $Co(NO_3)_2 \cdot 6H_2O$ without any use of a capping agent by a one-step hydrothermal method. Three kinds of Co_3O_4, a cube with the (001) plane, a truncated octahedron with (001) and (111) planes, and an octahedron with the (111) plane were reported.[30]

NiO crystals retained lithium storage capacity of 468 mAh g^{-1} at 20 C rate, and 322 mAh g^{-1} at 40 C rate, respectively.[28] The most stable crystal plane for NiO crystal is the (100) plane with the lowest surface energy of 0.958 J m^{-2}. The (110) and (101) planes have relatively high values, larger than 1.47 J m^{-2}. Because of the relatively high surface energy, the (110) crystal planes provide reactive sites for reaction with Li^+ ions, which can facilitate fast conversion reaction during the charge and discharge process. Likely, CuO single crystal with exposed high-energy (001) facets also shows high rate capability.[29]

A reversible discharge capacity as high as 815 mAh g^{-1} after the 200th cycle was delivered at a current density of 0.5 A g^{-1} when ultrathin nanosheets of Fe_2O_3 preferential exposure of (110) facets was used as the negative electrode material.[52] The highly exposed (110) facets of Fe_2O_3, largely dominated by the high density of Fe atoms, play an important role in the Fe/Li_2O interface. The Fe_2O_3 mesocrystals obtained by crystal facet engineering also show the improved cycling behavior.[53]

Electrochemical tests suggested that the electrochemical performance of Co_3O_4 is ranked as: octahedron > truncated octahedron > cube.[30] The (111) plane is more beneficial to Li^+ ion transport than the (001) plane. Co_3O_4 octahedra with (111) planes possessed the highest charge/discharge capacity and best cycling behavior. Through analyzing the surface atomic configurations in the (001), (111), and (110) planes of the Co_3O_4 unit cell, it can be clearly seen that the (001) plane contains only 2 Co(II) but the (111) plane contains 3.75 Co(III). There is a direct relationship between the electrochemical performance of Co_3O_4 and the redox reaction of Co^{m+}/Co. The Co_3O_4 octahedron has a larger area of exposed (111) planes and thus faster Co^{2+}/Co redox reaction. The authors also predicted that Co_3O_4 with (110) planes would exhibit better electrochemical performance than Co_3O_4 with (001) and/or (111) planes because the (110) plane contains 5 Co(II) and 4 Co(III) .

2.1.6 Other negative electrode materials with tailored facets

Apart from the above negative electrode materials, the effects of surface facet control are also clear for Li_3VO_4[15,16] and $Ca_2Ge_7O_{16}$.[54]

Hollow-structured Li_3VO_4 microboxes with exposed (200) plane was synthesized via in situ hydrothermal method reported by our group.[16] We found that the hollow Li_3VO_4 microboxes were formed via an oxygen-engaged oxidation process, as well as by Ostwald ripening. The low ratio of vanadium shows an enhancement in the (200) plane, as we can see from the peak intensity of the XRD pattern of the Li_3VO_4 (**Fig. 5a**). The trace oxygen dissolved in the solution may gradually oxidize V_2O_3 surface into VO_4^{3-}. Then reacting with LiOH, Li_3VO_4 precipitated on the surface could ensure that the surfaces of the V_2O_3 cubes are effectively covered, making the surface of a V_2O_3 cube less reactive than the freshly exposed interior. Actually, three lithium atoms and three oxygen atoms can form a radially arranged hexagon in the (100) plane (**Fig. 5b**), whereas two lithium atoms and two oxygen atoms can form a radially arranged rectangle in the (001) plane (**Fig. 5c**). Considering the diagonals of the hexagons and rectangles, the (100) plane has wider interatomic spacing for lithium. Therefore, lack of V cations could tend to increase the intensity of the (200) plane and decrease the intensity of the (002) plane. Similarly, Ostwald ripening process was also reported to grow $Ca_2Ge_7O_{16}$ nanowires with a preferred (001) growth direction.[54]

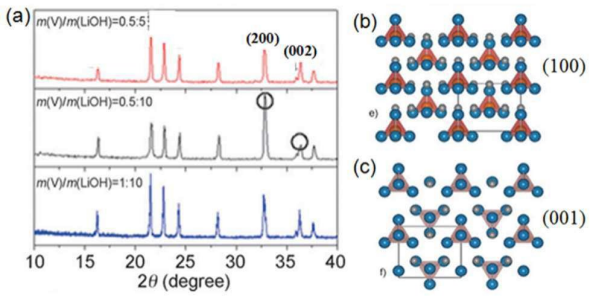

Fig. 5 (a) XRD patterns of Li_3VO_4 synthesized from different ratios of Li and V, structure of the orthorhombic Li_3VO_4 viewed from the (b) (100) plane and (c) (001) plane. The blue atoms are O atoms and the grey atoms are Li atoms. The atoms in the red tetrahedron cages are V atoms (modified from ref. 16, copyright permission from Wiley).

Li ions mainly intercalate into Li_3VO_4 in the potential range between 0.5 and 1.0 V (vs. Li^+/Li), lower than the potential of $Li_4Ti_5O_{12}$ and higher than that of graphite. Its theoretical capacity is 394 mAh g^{-1}, in accordance with in Li_5VO_4.[55] The Li_3VO_4 electrode with exposed (200) plane delivered a discharge capacity of 323 mA h g^{-1}, [16] close to that of commercial graphite [56] and much higher than that for $Li_4Ti_5O_{12}$ (in Section 2.1.2). It can also retain a reversible capacity of 83 mA h g^{-1} at 20 C. The $Ca_2Ge_7O_{16}$ nanowires with a preferred (001) growth direction exhibit a reversible capacities of 420 mA h g^{-1}.[54] It also shows an extremely long stable cycling. Actually, after the conversion reaction during the initial lithium uptake process, the in situ formed active Ge nanoparticles are highly dispersed within the mixed matrix of Li_2O and CaO, which not only provides an elastic buffer to accommodate the volume changes, but also prevents the agglomeration of nanosized Ge particles.

2.2 Positive electrode materials with tailored facets

The insertion or intercalation compounds are among the most useful positive electrode materials for Li ion battery, and some characteristics of them are summarized in **Table 2**.

Table 2 Some positive electrode materials with tailored facets and their primary characteristics.

Electrode	Tailored facets	Preparation method	Specific capacity /mAh g^{-1}	Rate /A g^{-1}	Cycle	Ref
$LiCoO_2$	(100)	Hydrothermal +calcination	189	1.4	200	57
$LiMn_2O_4$	(111)	Self-sacrifice template	115	3	500	58
$LiNi_{1/3}Co_{1/3}Mn_{1/3}O_2$	(010)	Precipitation +calcination	179	15C	100	59
$LiFePO_4$	(010)	Solvothermal method	164	20C	60	60
$Li_{1.2}Ni_{0.2}Mn_{0.6}O_2$	(010)	Precipitation +calcination	230	20C	80	61
$LiMnPO_4$	(010)	Hydrothermal method	130	0.5C	20	62

2.2.1 $LiCoO_2$ with tailored facets

For the past two decades, $LiCoO_2$ has been the dominant positive electrode material for commercial Li-ion batteries owing to its high energy density and long cycling life. [63] Although the theoretical capacity of $LiCoO_2$ is 274 mAh g^{-1}, its practical capacity is only around 140 mAh g^{-1} because its reversible amount of Li ion in $LiCoO_2$ is usually below 0.5 per unit. Over-delithiation will result in a phase transition from hexagonal to monoclinic phase, which leads to an abrupt shrinkage along the c-axis direction (9% volume change).[64]

$LiCoO_2$ has layered α-$NaFeO_2$ type structure (**Fig. 6a**).[65] By analyzing the crystal structure of $LiCoO_2$, it is obvious to find Li ions can fluently shuttle back and forth in the $LiCoO_2$ crystal along the [100] or [010] directions (**Fig. 6b and c**). Li ions are hard to diffuse in the crystal along [001] (**Fig. 6d**) because a mass of atoms such as oxygen or cobalt obstruct the passing route. Thus, the (010) and (100) planes perpendicular to the (001) plane are favorable for the transportation of Li^+ ion.

Uniform $Co(OH)_2$ nanoplates was synthesized by co-precipitation and then transformed into $LiCoO_2$ nanoplates by solid state reaction at 750 °C.[65] Al doped $LiCoO_2$ with the high exposing (100) plane was synthesized via solid state reaction with $Co_6Al_2CO(OH)_{16} \cdot H_2O$ and LiOH powder.[57]

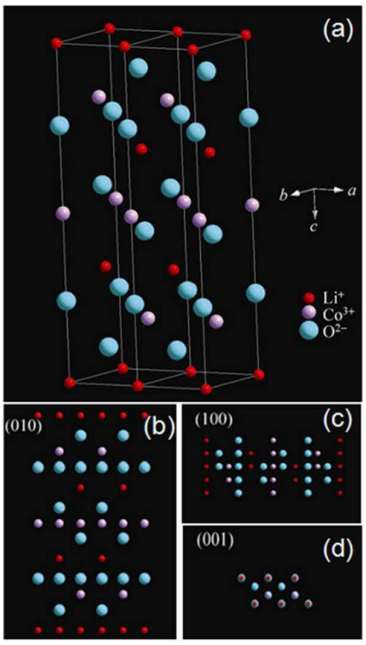

Fig.6 (a) The crystal structure of $LiCoO_2$ and perspective views from(b) (001), (c) (100) and (d) (001) planes, respectively (modified from ref. 65, copyright permission from Springer).

The initial discharge capacity of Al doped $LiCoO_2$ electrode is 189 mAh g^{-1} at 0.1C, higher than that of the conventional $LiCoO_2$.[57] After 200 cycles, it delivers a reversible capacity of 183 mAh g^{-1} (equal to 96.8% capacity retention). The Li ion rapid diffusion planes of (100) or their equivalent planes have tremendous large exposure ratio near to 100%, which remarkably improve the cycleability and rate capability of Al doped $LiCoO_2$. As discussed above, the (001) plane of $LiCoO_2$ is not electrochemically active. However, the $LiCoO_2$ nanoplates with exposed (001) plane present a stabile discharge capacity of 113 mAh g^{-1} at 1 A g^{-1} after 100 cycles.[65] It was found that there are many cracks on the nanoplates which are perpendicular to the (001) plane and favor fast Li^+ ion transportation.

2.2.2 $LiMn_2O_4$ with tailored facets

Spinel $LiMn_2O_4$, owing to its low cost, environmental friendliness, and the abundance of manganese resources, is regarded as one of the most prospective candidates for high-power positive electrode materials for Li ion battery.[66] Li ion extraction occurs at approximately 4 V (vs. Li^+/Li) in a two-stage process ($LiMn_2O_4/Li_{0.5}Mn_2O_4$ and $Li_{0.5}Mn_2O_4/\lambda$-MnO_2).[67] Further lithiation of $LiMn_2O_4$ occurs around 3 V (vs. Li^+/Li), which leads to the formation of rock salt phase $Li_2Mn_2O_4$. However, the dissolution of Mn easily happens in the spinel electrodes via a disproportionation reaction ($2Mn^{3+} \rightarrow Mn^{2+} + Mn^{4+}$) in the presence of acid impurities at high potential, which hurts its cycling stability.[68]

$LiMn_2O_4$ epitaxial films with (111) and (110) orientations was synthesized by pulsed laser deposition using $SrTiO_3$ (111) and (110) substrates, respectively.[69] $LiMn_2O_4$ nanosheets composed of single-crystalline with exposed (111) facets was synthesized via a template-engaged reaction using ultrathin MnO_2 nanosheets as self-sacrifice template.[58] Similarly, $LiMn_2O_4$ nanotubes,[70] nanorods[71] and nanowires [72] with exposed (110) planes were also prepared using the corresponding shaped MnO_2 as a self-sacrifice template.

Recently, structural changes of (111) and (110) surfaces for $LiMn_2O_4$ during the (de)intercalation process were reported. [69] It is suggested that the surface stability could be related to variations in the surface termination arrangements of oxygen ions and/or manganese ions with valence changing during redox reactions. As shown in **Fig. 7a**, the (111) plane of $LiMn_2O_4$ is terminated by a cubic closed-packed oxygen arrangement in the spinel structure while no closed-packed arrangement of oxygen appears in the (110) plane (**Fig. 7b**). The Mn ions are less densely arranged at the (110) surface and are easily in close contact with the electrolyte, which makes Mn ions highly reactive with solvents in the electrolyte. Therefore, (110) plane in the spinel $LiMn_2O_4$ structure is less stable than the (111) surface. However, the orientation of the (110) planes is obviously aligned to Li^+ ion diffusion, which can support fast Li ion insertion/extraction. So the above discussion may be the reason why all of the $LiMn_2O_4$ (nanotubes,[70] nanorods[71] and nanowires[72]) with (110) planes presents high-rate capabilities while $LiMn_2O_4$ nanosheet with exposed (111) facets exhibits good cycling behavior. For example, $LiMn_2O_4$ nanowires had a discharge capacity of about 80 mAh g^{-1} even at 150C (22.2 A g^{-1}) [72] while nearly 100% of the initial capacity could be retained after 500 cycles using the $LiMn_2O_4$ nanosheets with exposed (111) facets.[58]

Following the above idea, in order to obtain both excellent rate capability and cycling life, a truncated octahedral structure (**Fig. 7c**) was prepared through solid state reaction of lithium hydroxide monohydrate with an Mn_3O_4 truncated octahedron.[73] Its most surfaces are aligned to the orientation (111) planes activating minimal Mn dissolution, while a small portion of (110) planes are truncated along the directions that support Li ion diffusion. Octahedral structures enclosed by (111) planes (**Fig. 7d**) and nanoplates with even smaller dimensions (**Fig. 7e**) were also synthesized for comparison. The electrochemical test results (**Fig. 7f-h**) show that the truncated octahedral structure exhibits far better performance in both power density and cycle life compared to octahedral and panoplate structures. Therefore, the concept of truncating a small portion of surfaces to support Li ion diffusion while leaving most remaining surfaces aligned along the crystalline orientations with minimal Mn dissolution enables excellent rate performance and cycle life simultaneously.

2.2.3 $LiNi_{0.5}Mn_{1.5}O_4$ with tailored facets

The nickel-doped spinel-type material $LiNi_{0.5}Mn_{1.5}O_4$ is an attractive positive electrode candidate for next generation lithium-ion batteries as it offers high energy density with an operating voltage of 4.7 V (vs. Li^+/Li) involving the oxidation of Ni^{2+} to Ni^{4+}. [74,75]

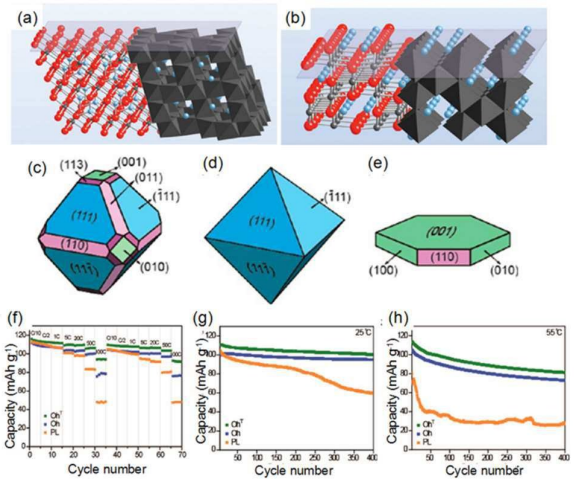

Fig. 7 Atomic stacking of $LiMn_2O_4$ along (a) (111) and (b) (110) orientations (modified from ref. 69, copyright permission from American Chemical Society); schematic illustration of $LiMn_2O_4$ with various crystal shapes for (c) truncated octahedron (Oh^T), (d) bare octahedron (Oh), (e) platelet (Pl), (f) their Rate capability measured at various discharge C-rates, and cycling behaviors at 10C for discharge at (g) 25 and (h) 55 °C (modified from ref. 73, copyright permission from American Chemical Society).

In contrast to the results from $LiMn_2O_4$ with (110) plane, [70-72] the truncated $LiNi_{0.5}Mn_{1.5}O_4$ sample with the presence of (110) planes exhibits poor electrochemical performance while the octahedral $LiNi_{0.5}Mn_{1.5}O_4$ material with high exposure of (111) planes demonstrates the highest reversible capacity and the best rate capability.[76] From the analysis in the above sections, we know that (111) plane in the spinel structure is more stable than the (110) planes while (110) planes can support fast Li ion insertion/extraction. So the electrochemical properties of $LiNi_{0.5}Mn_{1.5}O_4$ are very sensitive to the dissolution of Mn(III). Actually, most prepared $LiNi_{0.5}Mn_{1.5}O_4$ still contains a small amount of Mn(III), which can be evidenced by the small redox peak at 4.0 V (vs. Li^+/Li). The Mn ions are less densely arranged at the (110) surface, which are easy to be in close contact with the electrolyte, which makes the Mn ions highly reactive with solvents in the electrolyte.

2.2.4 $LiNi_{1/3}Co_{1/3}Mn_{1/3}O_2$ with tailored facets

$LiNi_{1/3}Co_{1/3}Mn_{1/3}O_2$, as another commercial positive electrode material, has a more stable structure than the basic layered oxides such as $LiCoO_2$, $LiNiO_2$ and $LiMnO_2$.[77,78] In $LiNi_{1/3}Co_{1/3}Mn_{1/3}O_2$, divalent nickel ions and trivalent cobalt ions are electroactive, involving Ni^{2+}/Ni^{4+} and Co^{3+}/Co^{4+} redox couples. Electrochemical inactivity of tetravalent manganese ions benefits the structure stability and effectively prohibits capacity fading.

$LiNi_{1/3}Co_{1/3}Mn_{1/3}O_2$ with a hexagonal α-$NaFeO_2$ layer structure, which is similar to that of $LiCoO_2$, is made up of MO_2 oxygen layers perpendicular to the c axis, indexed to (001) facets that include the (001) and (001) planes at the top and bottom.[59] The close packed (001) facets are therefore not electrochemically active for Li^+ ion transportation due to the close-packed structure. The (010) facets are perpendicular to the (001) facets and have an open structure with a wide window between the layers for Li^+ ion migration. Therefore, producing $LiNi_{1/3}Co_{1/3}Mn_{1/3}O_2$ crystals with a high percentage of exposed (010) facets will facilitate the fast and efficient transportation of Li^+ ion.

Single crystalline $LiNi_{1/3}Co_{1/3}Mn_{1/3}O_2$ nanobricks with a high percentage of exposed (010) facets were synthesized by a solid-state reaction of $LiOH{\cdot}H_2O$ and nickel-cobalt-manganese hydroxide precursor.[59] When the plate-like structure is formed, PVP molecules immediately adsorb on its negatively charged (001) surfaces via the amine groups, thus reducing the growth rate along the (001) direction and leading to the formation of (001)-plane-dominated nanoplates. Then, the produced precursor $Ni_{1/3}Co_{1/3}Mn_{1/3}(OH)_2$ was mixed with lithium salt and calcined at high temperature. The $Ni_{1/3}Co_{1/3}Mn_{1/3}(OH)_2$ hexagonal nanosheets with the reaction of Li salt along the (010) direction result in a significant increase in the percentage of lateral (010) facets. Besides, a polyol medium (ethylene glycol) can also be used to control the preparation of the $LiNi_{1/3}Co_{1/3}Mn_{1/3}O_2$ nanoplates with exposing (010) active facets.[79] Hierarchical cubed $LiNi_{1/3}Co_{1/3}Mn_{1/3}O_2$ with enhanced growth of (010) facets was synthesized by using cube structured $MnCO_3$ as a self-sacrifice template. [80]

In case of single crystalline $LiNi_{1/3}Co_{1/3}Mn_{1/3}O_2$ nanobricks with a high percentage of exposed (010) facets, the initial discharge capacities are 159, 151, 136 and 130 mA h g^{-1} at 2, 5, 10 and 15 C rates, respectively.[59] Both $LiNi_{1/3}Co_{1/3}Mn_{1/3}O_2$ nanoplates and microcubes with exposed (010) active facets display a high initial discharge capacity of above 200 mAh g^{-1} at a low current density.[79,80] All of them exhibited excellent cycling behaviors. Moreover, the $LiNi_{1/3}Co_{1/3}Mn_{1/3}O_2$ crystalline with a high percentage of exposed (010) facets also ensured an ordered atomic arrangement, which improves the stability of the crystallographic structure upon cycling.[59]

2.2.5 $LiFePO_4$ with tailored facets

The olivine-structured lithium iron phosphate ($LiFePO_4$) is also good positive electrode material for commercial usage in Li-ion battery because of its high theoretical capacity (172 mAh g^{-1}), the one dimensional diffusion channel along the (010) direction, excellent safety attribute, attractive cost competitiveness and environmentally benign. [81-85] However, $LiFePO_4$ is a poor conductor of both electrons and Li^+ ions. [82,83]

Many theoretical calculations and atomistic models were applied to study the surface energy of $LiFePO_4$ structure. Through studying the Li^+ ion transportation in olivine $LiFePO_4$ by first-principle calculations, it was found that the (010) plane possesses a lower Li ion migration energy and higher Li ion diffusion coefficient, up to several orders of magnitude than that for (001) plane. [86] Therefore, considerable attempts have been made to enhance their electrochemical performances by construction of $LiFePO_4$ materials with maximal exposure of

(010) plane over other ones. Solvothermal and hydrothermal reactions are two effective strategies to prepare $LiFePO_4$ with an increased percentage of (010) planes.[60, 87-90] The selection of chelating agent, reaction temperature and time, composition and concentration of surfactant play critical roles in the growth of $LiFePO_4$ nanocrystals.

The $LiFePO_4$ nanoplates with exposure of different crystal planes of (010) and (100) demonstrate similar discharge capacities at low current densities but quite different ones at high current densities (5 and 10C-rates).[60] For example, $LiFePO_4$ nanoplates with (010) planes delivered 156 and 148 mAh g^{-1} at 5 and 10 C-rates, respectively, while the latter delivered 132 and only 28 mAh g^{-1} at 5 C-rate and 10 C-rate, respectively. It was reported that crystallographic plane of the $LiFePO_4$ nanoplates was controlled by the mixing procedure of the starting materials. In addition, the b-axis thickness plays a critical role in the percentage of (010) planes and the electrochemical performance of the $LiFePO_4$. With a decreased b-axis thickness, the $LiFePO_4$/C nanoplates present increasingly improved electrochemical properties in comparison with those of larger b-axis thickness, owing to the higher percentage of (010) planes than those of smaller b-axis thickness.[88] The key point is to allow $LiFePO_4$ to grow along the ac plane and decrease the thickness of the b-axis as much as possible, leading to more exposure of (010) planes.

2.2.6 $xLi_2MnO_3 \bullet (1-x)LiMO_2$ or $Li(Li_{1/3-2x/3}M_xMn_{2/-x/3})O_2$ (M = Mn, Ni,Co, Fe, Cr, etc.) with tailored facets

Lithium-rich layered oxide materials, $xLi_2MnO_3 \bullet (1-x)LiMO_2$, have attracted much attention in recent years because their capacities can be larger than 250 $mAhg^{-1}$.[91, 92] However, the low initial coulombic efficiency, unsatisfied rate performance and cycling stability of these materials are still the main problems preventing their utilization in practical Li-ion batteries.[93] Due to the removal of oxygen above 4.5 V (vs. Li^+/Li), this kind of positive electrode material usually suffers from a huge irreversible capacity loss and rearrangement of surface microstructure.[94]

The benefits of faceting have also been observed for lithium-rich layered oxide materials. In this positive electrode material with α-$NaFeO_2$ structure, it was widely reported that Li^+ ion prefers to intercalate along the direction parallel to the Li^+ ion layers, as discussed in 2.2.1 and 2.2.4 sections. The (010) facets can facilitate the migration of Li^+ ion between the MO_6 octahedra interlayers. Two different synthetic approaches were employed to synthesize lithium-rich layered oxide materials with deliberately (010) planes.[62,95] It has been demonstrated that a different precursor and a shorter hydrothermal time both enable the $Li_{1.17}Ni_{0.25}Mn_{0.58}O_2$ nanoplates to grow simultaneously along the (010) and (001) direction, leading to the formation of (010)-facet-dominated nanoplates.[95] Another layered lithium-rich material, hierarchical $Li_{1.2}Mn_{0.6}Ni_{0.2}O_2$ quasi-sphere whose surface is constructed with (010) planes, were prepared by using $Ni_{0.2}Mn_{0.6}(OH)_{1.6}$ precursors as a self-sacrifice template.[61] The hierarchical nanostructured $Ni_{0.2}Mn_{0.6}(OH)_{1.6}$ precursors were synthesized through a co-precipitation reaction. After heat-treatment with the lithium salts at 900 °C, the nanoplates are developed with rounded edges, shrunk lateral dimension, and expanded thickness, leading to a decrease in the non-electrochemically active (001) facets.

At 6C-rate, the reversible capacity of $Li_{1.17}Ni_{0.25}Mn_{0.58}O_2$ nanoplates could reach around 200 mAh g^{-1}, and 186 mA h g^{-1} after 50 cycles. [95] In comparison with that in conventional thermodynamic equilibrium nanoplate material of lithium-rich layered oxide materials, the active surface area in this habit-tuned nanoplate material of $Li_{1.17}Ni_{0.25}Mn_{0.58}O_2$ sample is increased by about 50% although the proportion of the (010) nanoplates is only about 1/7. The hierarchical structured $Li_{1.2}Mn_{0.6}Ni_{0.2}O_2$ yields high initial specific discharge capacities of 230.8 and 141 mAh g^{-1} at 1C and 20C rate, respectively, demonstrating an outstanding high-rate performance,[61] which is attributed to the increased active surface area for Li^+ ion transportation in the lithium-rich layered oxide. This unique hierarchical structure combines the advantages of a hierarchical architecture with electrochemical active (010) planes. The special directional alignment of nanoplates provides paths for Li^+ ion rapid insertion/extraction, while the hierarchical structure gives efficient 3D electron transport network, which enables both efficient ion and electron transport for fast Li^+ ion transport kinetics.

2.2.7 Other positive electrode materials with tailored facets

$LiMnPO_4$, one member of the phosphate olivines, is also a promising positive electrode material with a higher intercalation potential at 4.1 V (vs. Li^+/Li) than that of $LiFePO_4$. However, $LiMnPO_4$ also suffers intrinsically low electronic conductivity (< 10^{-10} S cm^{-1}) and sluggish Li ion diffusion in the bulk resulting in poor rate performance. [96] Since the 1950s, a class of the polyanionic materials such as Li_2MSiO_4 (M = Mg, Zn, Ca, Co, Fe, and Mn) have been intensively studied as a glass-ceramics materials for traditional ceramics industry. Among these materials, Li_2FeSiO_4 and Li_2MnSiO_4 were studied as positive electrode materials for Li-ion batteries.[97,98]

$LiMnPO_4$ microspheres with different crystallographic orientations were assembled via a facile hydrothermal route.[62] $Na_2S{\cdot}9H_2O$ is employed as a sole additive for controlling the phase, shape and crystallographic orientation of $LiMnPO_4$ microspheres. $Na_2S{\cdot}9H_2O$ additive can be rapidly hydrolyzed into sulphion and hydroxyl ions which selectively adsorb on different crystallographic facets of a $LiMnPO_4$ crystal in aqueous solution. Li_2FeSiO_4 and Li_2MnSiO_4 nanosheets with growth oriented along the a-axis were prepared by a rapid one pot supercritical fluid synthesis method.[99] The surface tension of supercritical fluids completely vanishes above the critical point of the fluid, which is of particular utility in controlling the surface and interface chemistries of the nanostructured materials.

The synthesized $LiMnPO_4$ microspheres assembled with nanoplates exhibit discharge capacities of 130 mAh g^{-1} at 0.05 C and 76.8 mA h g^{-1} at 0.5 C, respectively, which had a superior electrochemical performance over microspheres assembled

with edges and prisms.[62] This is due to the exposure of (010) facets. The (010) direction is the thinnest part of the crystal allowing for fast Li^+ ion diffusion. Ultrathin Li_2MnSiO_4 nanosheets show a discharge capacity of 340 mAh g^{-1}. [99] For the first time, two Li ions were successfully extracted/inserted using the Li_2MnSiO_4 nanosheets. The sheet-like morphology oriented along the a-axis has a significant effect on achieving the two Li ion insertion/extraction of the Li_2MnSiO_4. The orthorhombic and monoclinic structures of the Li_2MSiO_4 family are both based on slightly distorted hexagonal close packing of oxygen ions with all cations in tetrahedral voids and a pseudohexagonal plane parallel to (001).

3 Electrode materials with tailored facets for aqueous rechargeable lithium batteries

The experience from Li-ion batteries technology shows that the use of flammable organic electrolytes might lead to thermal run-away and safety accidents. Moreover, the cost of Li-ion battery is relatively high due to the organic electrolytes and special cell assembly technology such as the requirement of a strictly dry environment during manufacturing processes. In this regard, aqueous rechargeable lithium batteries (ARLBs) were proposed in 1994.[100] However, the inferior capacity retention and low energy density limit their practical application. In 2007, ARLBs using various electrode materials based on redox reactions were reported by our groups and have attracted wide attention as a promising system in the past several years. [101] ARLBs can overcome some disadvantages of Li-ion batteries. It is inherently safe by avoiding the use of flammable organic electrolytes. Moreover, the cost of the aqueous electrolyte is low because the expensive salts can be replaced by cheap ones. In addition, the ionic conductivity of aqueous electrolytes is high, about two orders of magnitudes higher than that of organic electrolytes, which ensures high rate capability and thus high specific power.[102-104]

3.1 Negative electrode with tailored facets

As for the negative electrode materials of ARLBs, vanadium oxides, molybdenum oxides and some lithium intercalation compounds have been reported. Among them, LiV_3O_8,[105] $H_2V_3O_4$ [106] and VO_2 [107] with referred orientation and exposure of facets were studied in the past several years.

Hierarchical LiV_3O_8 nanofibers, assembled from nanosheets that have exposed (100) facets, were fabricated by using electrospinning combined with calcination.[105] During calcination, PVA was used and decomposed to release CO_2, whilst NH_4VO_3 reacted with $Li(CH_3COO)\cdot H_2O$ to produce LiV_3O_8 nanoparticles. Besides acting as the template for forming the fibers, PVA could prevent LiV_3O_8 nanoparticles from aggregating into larger ones, making them grow into small nanosheets with exposed (100) facets owing to the self-limitation property of LiV_3O_8. Single-crystal $H_2V_3O_8$ nanowires along the [001] growth direction were obtained through a facile method by one-step hydrothermal treatment of commercial V_2O_5 powder.[106] Flowerlike VO_2 (B) micro-nanostructures assembled by single-crystalline nanosheets have been successfully synthesized via a hydrothermal route using polyvinyl pyrrolidone (PVP) as a capping reagent.[107]

Compared with the other LiV_3O_8 micro/nanostructures, the hierarchical LiV_3O_8 with exposed (100) facets clearly possesses better electrochemical performance in ARLBs. When the pH value of the electrolyte was adjusted to below 5, it was found that nanosheets with exposed (100) facets could effectively alleviate proton co-intercalation into the LiV_3O_8 electrode. In the crystal structure of LiV_3O_8, the (010) and (001) facets provide a lot of channels while the (100) facet has fewer and smaller channels, which makes it more difficult for H^+ ions to intercalate into this material. A small amount of H^+ ions intercalating into these channels instead of Li^+ ions will lead to capacity fading. The pH value of the electrolyte has few influence on the cycling performance of the hierarchical LiV_3O_8 nanofibers with exposed (100) facets. [105]

The post-treated flowerlike VO_2 (B) electrode shows an initial discharge capacity reaching 81 mAh g^{-1}, which is higher than that of the flowerlike VO_2 (B) sample before annealing.[107] Compared to V_2O_5, $H_2V_3O_8$ (or $V_3O_7\cdot H_2O$) has a higher electronic conductivity arising from a mixed-valence of V^{4+}/V^{5+}. The $H_2V_3O_8$ nanowires allow a full intercalation of Li^+ ion in preference to hydrogen evolution, thus can deliver a specific capacity of 234 mAh g^{-1},[106] much higher than that of any other vanadium oxides (VO_2 [107] and V_2O_5 [108]) in aqueous electrolyte. In $H_2V_3O_8$, the V_3O_8 layers are held together by van der Waals interactions together with hydrogen bonding, in which this weakly-bonded layer structure can favor the mobility of Li^+ ion between the layers.

3.2 Positive electrode with exposed facets

As discussed in Section 2.2, intercalation compounds ($LiCoO_2$, $LiNi_{1/3}Co_{1/3}Mn_{1/3}O_2$, $LiMn_2O_4$ and $LiFePO_4$) are used as positive electrode materials for lithium ion batteries. In aqueous electrolytes, lithium intercalation and de-intercalation can also occur in/from these materials like in organic electrolytes.

$LiMn_2O_4$ nanotube with a preferred orientation of (400) planes was prepared by using multiwall carbon nanotubes as a sacrificial template. [12] The orientated MnO_2 was deposited on the CNTs. Then the as-prepared $LiMn_2O_4$ kept a typical crystal orientation after reacting with Li salt at 700 °C. In the standard $LiMn_2O_4$, the intensity of (111) planes is much stronger than that of (400) ones. [66,68] For the prepared $LiMn_2O_4$ nanotubes, their intensities are almost the same, suggesting that the $LiMn_2O_4$ has a crystal orientation. $LiFePO_4$ crystal with major exposure of (010) facets was prepared by reflux route in ethylene glycol solution under atmospheric pressure. [13]

Both $LiMn_2O_4$ with a preferred orientation of (400) facets and $LiFePO_4$ crystal with major exposure of (010) facets present superfast second-level charge capability (up to 1000C).[13,65] In case of the crystal orientation of the $LiMn_2O_4$ nanotube, there are more (001) or (010) planes on the edges of these planes or vertical to (400) planes which is similar to the $LiCoO_2$ nanoplates with exposed (001) plane.[65] The 8a sites for lithium intercalation

and deintercalation are situated at the (001) or (010) planes. Therefore, more Li sites are exposed to the aqueous electrolyte due to the preferred growth of (400) planes.

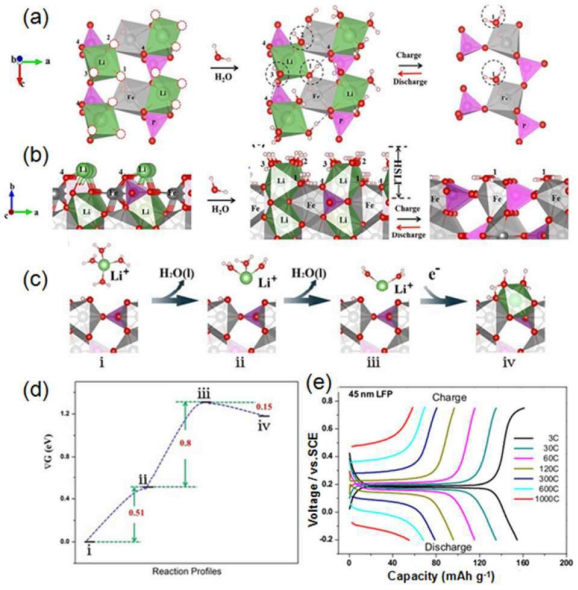

Fig. 8 (a) Top (b) side views of $LiFePO_4$/vacuum, $LiFePO_4/H_2O$, and $FePO_4/H_2O$ at (010) direction. The four LiO_6 octahedrons correspond to four Li diffusion channels. The dashed red cycles denote the O vacancies at the surface. (c) The reaction profiles for Li^+ ions transport across the $FePO_4$/water interface in the discharge process and (d) their energies at each step (right hand panels). (e) Charge and discharge curves at different current density (1 C = 170 mA g^{-1}) between 0.2 and 0.75 V vs. SCE in 0.5 M Li_2SO_4 aqueous electrolyte (modified from ref. 13, copyright permission from American Chemical Society).

As for $LiFePO_4$ with exposure of (010) facets, the reason for fast charge in aqueous electrolyte is a little relatively complicated. The H_2O adsorption at different atomic sites on $LiFePO_4$ (010) surface was calculated and the most stable structure was identified when three H_2O molecules adsorb at three different sites, as illustrated in **Fig. 8a** and **b** (the 1, 2, 3 sites). These sites are the exact locations of the O vacancy at the corners of FeO_6 and LiO_6 octahedrons in a stoichiometric (010) $LiFePO_4$ surface. Such unique arrangement of water molecules at those $LiFePO_4$ (010) sites was verified with an accurate in situ mass measurement (EQCM) and Fourier transform infrared spectroscopy (FTIR). Each Li^+ ion in aqueous electrolyte is always coordinated by 4 water molecules in its primary solvation sheath. Two water molecules will be stripped away from this complex in order for a Li^+ ion to intercalate into the nanoparticle (i to ii, and to iii in **Fig. 8c** and **d**). Then the resultant $Li^+(H_2O)_2$ can approach the $LiFePO_4$ surface with almost no additional barrier and docks at the site (iii to iv in **Fig. 8 c** and **d**) to form a structure similar to the scenario of $3H_2O$ on top of $LiFePO_4$ in **Figure 9b**. Such interfaces (HSLE) are effective in promoting fast mass transfer, which bring about high rate capability (**Fig. 8e**). After this Li^+ ion diffuses into the $LiFePO_4$ bulk along the Li channel, these two H_2O will desorb from the surface.

4 Electrode materials with tailored facets for Na-ion battery

Historically, progress in Na-ion batteries is parallel to that of lithium ion batteries.[109] Unfortunately, Na-based systems rapidly fell into oblivion because Na^+ ions are much larger in radius than Li^+ ions and it is more difficult to find a suitable host material to accommodate Na^+ ions. However, for sustainability reasons, the Na-ion batteries have recaptured the scientific community's attention in recent years. The breakthroughs in material science open new horizons for new energy storage and conversion devices. [110]

4.1 Negative electrode with exposed tailored facets

In this section, recent research progress on negative electrodes with tailored facets for Na ion battery is summarized, like SnO_2 octahedral nanocrystals consisting of dominantly exposed (221) high energy facets,[111] SnO nanocrystal exposed with (001) facets.[112]

SnO_2 with exposed (221) high energy facets and SnO with exposed (001) facets were synthesized by hydrothermal method using PVP and Na_2SO_4 as morphology directing agent, respectively.[111,112] Sulfate ions are most strongly adsorbed to faces perpendicular to the c-axis of the crystal through bridging-bidentate adsorption, leading to the retarded growth along the c-axis and the formation of the facet crystals. [112]

SnO_2 nanocrystals with exposed (221) facets demonstrated a good high rate performance.[111] It was found that Na ions first insert into SnO_2 crystals at the voltage range from 3 to 0.8 V (vs. Na^+/Na), and that the exposed (1 × 1) tunnel-structure could facilitate the initial insertion of Na ions. Then, Na ions react with SnO_2 to form Na_xSn alloys and Na_2O in the low voltage range from 0.8 to 0.01 V (vs. Na^+/Na). The SnO with exposed (001) facets electrodes delivered specific capacities of 525, 438, and 421 mA h g^{-1} at current densities of 40, 80, and 160 mA g^{-1}, respectively.[112] Similar to SnO_2, SnO nanocrystals are dominated by (001) facets, exposing the 2D diffusion pathways for the insertion of Na^+ ions into SnO crystals and the facilitated reaction towards sodium at high current densities.

4.2 Positive electrode with tailored facets

Positive materials are considered in this section including V_2O_5 hollow nanospheres constructed from hierarchical nanocrystals with predominantly exposed (110) crystal facets.[113] $Na_{0.54}Mn_{0.50}Ti_{0.51}O_2$ with growth direction perpendicular to the c-axis,[114] $Na_{0.7}MnO_2$ single crystals predominantly exposed their (100) facets [115] and β-MnO_2 nanorods with exposed (111) crystal facets.[116]

V_2O_5 with predominantly exposed (110) crystal planes was synthesized via a polyol-induced solvothermal process.[113] The preferred orientation of V_2O_5 nanocrystals is not triggered by the preparation conditions, but influenced by the vanadyl

ethylene glycolate precursor's crystal structure. Tunnel-structured $Na_{0.54}Mn_{0.50}Ti_{0.51}O_2$ nanorods were synthesized by a facile molten salt method.[114] These nanorods are grown in the direction normal to the Na-ion tunnels, which could greatly shorten the diffusion distance of Na ions and benefit the transference kinetics. The $Na_{0.7}MnO_2$ nanoplates with exposed (100) crystal plane and β-MnO_2 nanorods with exposed (111) crystal planes were synthesized by a hydrothermal method.[115,116] The individual $Na_{0.7}MnO_2$ nanoplate shows the perfect rhombus shape. Its corresponding SAED spot pattern could be well-indexed to the orthorhombic crystal structure along the (100) zone axis. And the facet vertical to the incident electron beam is the (100) crystal plane. The two basal planes of the rhombus nanoplates are the (100) facets, which are the predominantly exposed facets. For the $Na_{0.7}MnO_2$ with layer structure, each layer perpendicular to the c axis is indexed as the (001) crystal plane. The (001) crystal plane is not electrochemically active for Na^+ ion transport while (100) crystal plane is an active plane for Na^+ ion insertion/extraction, owing to the existence of a 2D channel for Na^+ ion transport. So the $Na_{0.7}MnO_2$ nanoplates with predominantly exposed (100) facets could easily take place the insertion/extraction of Na^+ into/from the crystal structure. At a current density of 0.18 A g^{-1}, the $Na_{0.7}MnO_2$ nanoplate electrode still delivers an initial capacity of 125 mA h g^{-1}.[115]

Beta-MnO_2 nanorods delivers a high initial discharge capacity of 350 mAh g^{-1}. Although the discharge capacity decreases gradually upon cycling, it still maintains a high specific capacity of 200 mAh g^{-1} after 100 cycles.[116] These β-MnO_2 nanorods have exposed (111) crystal planes with a high density of (1 × 1) tunnels. The (1 × 1) tunnel not only provides facile transport for Na-ion insertion and extraction but also accommodates Na-ions.

5 Electrode materials with tailored facets for Li-O_2 battery

The Li-O_2 battery was first introduced in 1996, and it was composed of a lithium, an organic-impregnated polyacrylonitrile electrolyte, and a carbon electrode.[117] A decade later, the Li-O_2 battery used organic carbonates as the electrolyte was demonstrated.[118] After that, research on Li-O_2 batteries quickly became a hot topic.[119-121] A typical rechargeable non-aqueous Li-O_2 battery is comprised of a Li metal as the negative electrode, a Li conducting organic electrolyte and a catalyst with oxygen as positive electrode. Catalytic processes critically depend on the surface atoms' arrangement and the number of dangling bonds on different crystal planes.

The catalytic properties of polyhedral Au nanocrystals (NC) with different index facets were studied in Li-O_2 battery, including cubic gold (Au) NCs enclosed by (100) facets, truncated octahedral Au NCs enclosed by (100) and (110) facets, and trisoctahedral (TOH) Au NCs enclosed by 24 high-index (441) facets.[122] This preparation system has three species including the reducing agent (ascorbic acid), the gold precursor ($HAuCl_4$) and the capping agent (surfactant: CTAB or CTAC). It has been found that CTAB molecules can bind more strongly to the (100) than the (111) facets.[123] Different CTAB concentration conditions can produce shapes with (100) or (111) faces. When CTAB is replaced by CTAC at the same concentration for the synthesis, TOH Au NCs bounded by (441) facets dominate in the final product. The controllable synthesis of Co_3O_4 with different shape and crystal planes and their catalytic properties for Li-O_2 batteries have also been systematically studied, including nanocubes, pseudo octahedrons, nanosheets, hexagonal nanoplatelets and nano-laminar.[124] They are exposed with (100), (110), (111), and (112) crystal facets, respectively.

Compared to the carbon black (Super-P, SP), all these Au NCs significantly reduce the charge potential and show high reversible capacities (**Fig. 9**). Particularly, TOH Au NC catalysts demonstrate the lowest charge/discharge overpotential and the highest capacity of 20298 mA h g^{-1}. Density function theory calculations on the different Au crystal planes and their interaction with the Li and O atoms show that the interaction energy between the Au and the Li and O atoms decreases as the surface energy of the Au crystal planes increases. The oxygen adsorption energy on the surface of the (441) crystal planes is lower than those of the (100) and (111) crystal planes, which makes TOH Au NCs more active toward the oxygen evolution reaction (OER), thus leading to an enhanced electrochemical performance.[122]

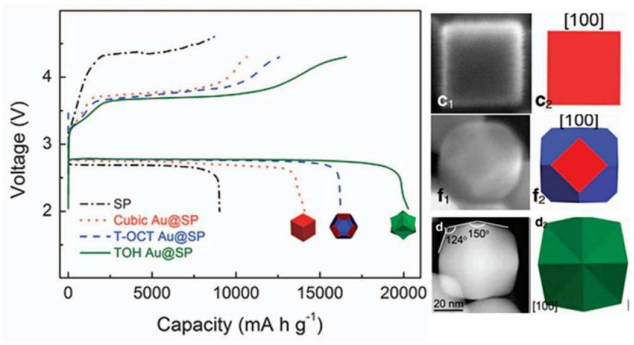

Fig. 9 Charge-discharge curves of the cubic Au NCs@SP (red line), T-OCT Au NCs@S P (blue line), TOH Au NCs@SP (green line) and bare SP electrodes (black line) at 100 mA g^{-1} in the first cycle. The right images are their FEM or TEM micrographs and structure models (modified from ref. 122, copyright permission from Nature Publishing Group).

For Co_3O_4 catalyst, the essential factor to promote the OER is also its surface crystal planes.[124] The correlation of different Co_3O_4 crystal planes and their effect on reducing charge-discharge over-potential is established in the following order: (111) > (112) > (110) > (100). Similar to the above Au crystal planes, Co_3O_4 (111) crystal planes with highest surface energy have the largest interaction with Li and O atoms, leading to the highest catalytic property for the Li and O reaction.

6 Electrode materials with exposed facets for supercapacitors

Supercapacitors have some advantages over batteries such as short charge-discharge time, high power density, high charge-discharge efficiency and long cycling life. According to different charge-storage mechanisms of electrode materials, supercapacitors can be categorized into electrochemical double layer capacitors (EDLCs) and Faradaic pseudocapacitors. [125,126] In terms of electrode configuration, supercapacitors can be fabricated as symmetric and asymmetric supercapacitors. The well-studied materials for EDLCs are usually based on nanostructured carbon materials. Pseudocapacitive materials cover transition metal oxides, conducting polymers and intercalation compounds. Among them, carbon materials and conducting polymers are amorphous, so these electrode materials are not including in this section.

6.1 Negative electrode with tailored facets

Hierarchical nanotubular titanium nitride (TiN) was fabricated by magnesiothermic reduction of titania replicas of ordinary filter paper (cellulose substance).[127] The preferred growth direction is perpendicular to [200]. The Fe_3O_4@SnO_2 core/shell nanorod film was achieved by fabricating Fe_3O_4 pristine nanorod film from FeOOH followed by the hydrothermal coating with SnO_2 nanoparticles.[128] Fe_3O_4 nanorods possess a single-crystal nature and grow along the [110] direction. MoO_3 nanoplates with a crystal orientation along [001] were prepared via a sol-gel method in our group. [129] The prepared MoO_3 consists of nanoplates which are on average about 1 μm × 1 μm × 100 nm. A core/shell structure of PPy grown on V_2O_5 nanoribbons was fabricated by using SDB^- (dodecylbenzenesulfonate) as a surfactant in our group.[130] The V_2O_5 nanoribbons were prepared by hydrothermal treatment of NH_4VO_3 and poly(ethylene oxide)-block-poly(propylene oxide)-block-poly(ethylene oxide) copolymer in acid solution at 120 °C.

TiN possesses attractive properties like thermal conductivity, corrosion resistance and chemical stability. Its shape of the CV curve is approximated to rectangular in 1 M KOH electrolyte, which is an ideal double layer capacitive behavior.[127] The specific capacitance of TiN was very low, only 74.2 F g^{-1} at 0.16 A g^{-1}. When Fe_3O_4@SnO_2 core/shell nanorod film is tested in the potential range of -0.8-0.2 V (vs. Ag/AgCl) in 1 M Na_2SO_3 solution, 82.8% of the initial capacitance could be stabilized after 2000 cycles.[128] It is claimed that the capacitance of magnetite Fe_3O_4 is originated from the surface redox reaction of sulfur in the form of sulfite anions, as well as the redox reactions between Fe^{2+} and Fe^{3+} accompanied by intercalation of sulfite ions to balance the extra charge with the iron oxide layers. Besides, the SnO_2 absorbs solvated cations (Na^+) on the electrode surface from the electrolyte.

The MoO_3 nanoplates with a crystal orientation along [001] have a specific capacitance of 280 F g^{-1} in Li_2SO_4 aqueous electrolyte, which is higher than that for the bulk MoO_3 (208 F g^{-1}).[129] The nanoplate structure makes the solvated Li^+ ions reach the MoO_3 surface more easily than the bulk MoO_3. Our group also investigated insertion/extraction of K^+ ions into/from V_2O_5 occurring in the (00l)-planes-constituted interlayer space.[130] V_2O_5 retains a layered structure with distinct diffraction peaks of (001), (003), and (004) planes. When K^+ ions insert into the V_2O_5 electrodes possessing K/V ratio of 0.35, the calculated interlayer space of (001) plane decreases to 9.45 Å in comparison with the original value of 10.5 Å. This is probably resulted from the reinforced interaction between K^+ and the V_2O_5 skeleton. At the end of charge and discharge, the interlayer space expands slightly at the end of the charge accompanied by K^+ ion extraction. The specific capacitance of V_2O_5 nanoribbons is 162 F g^{-1} at 100 mA g^{-1}. The PPy shell coated on the V_2O_5 core further improves the charge transfer process and prevents vanadium dissolution into the aqueous electrolyte.

6.1 Positive electrode with tailored facets

The capacitance of Co_3O_4 is directly linked to surface properties and its electrochemical performance is greatly influenced by any change related to the surface morphology of this electroactive material.[131] A Co_3O_4@CNT hybrid was in situ prepared by depositing Co_3O_4 on CNTs through a simple hydrothermal method. The size of the Co_3O_4 nanoparticles with preferred exposed (220) planes is 10 – 15 nm.[132] Co_3O_4 nanomesh with large-scale exposed (112) crystal plane is obtained based on the formation of single-crystal $(NH_4)_2Co_8(CO_3)_6(OH)_6{\cdot}4H_2O$ nanosheet as the precursor and its subsequent conversion upon heating in air.[133] The monocrystallization and conversion process from $(NH_4)_2Co_8(CO_3)_6(OH)_6{\cdot}4H_2O$ to Co_3O_4 is considered as thermodynamically supported recrystallization. The exposed crystal plane of Co_3O_4 on the largest scale is changed from (110) to (112) with the precursors changing from $Co(CO_3)_{0.5}(OH)_{0.11}{\cdot}H_2O$ to $(NH_4)_2Co_8(CO_3)_6(OH)_6$-$4H_2O$, which is convinced by XRD measurements.

NiO hexagons with exposed (110) facets on metallic Ni backbones were prepared via a simple hydrothermal method followed by annealing at 300 °C for 1 h.[134] The presence of SO_4^{2-} anions in the solution is primarily responsible for the restricted crystal growth in the perpendicular direction as they are strongly adsorbed onto the surfaces perpendicular to the c-axis through bridging-bidentate adsorption, thereby resulting in oriented hexagonal nanoplatelets of $Ni(OH)_2$ on the surface. Upon annealing, the hexagon shapes are preserved and the exposed facets are the (110) ones which allow a lower lattice mismatch with $Ni(OH)_2$. The NiO crystals have dominantly exposed (110) facets on both the hexagonal surfaces together with (002) and (111) facets as edges, forming a close-packed hexagonal nano platelet structure.

Alpha-MnO_2 nanowires grown on flexible carbon fabric were synthesized by a hydrothermal approach.[135] The growth direction of this MnO_2 nanowires is very close to the normal direction of the (112) plane. Mn_3O_4 octahedral nanoparticles with (101) facets was prepared by a simple controlled oxidation method,[136] similar to the growth mechanism of Li_3VO_4.[15,16] Mn_3O_4 exists naturally as hausmannite, a distorted spinel in which Mn(II) and Mn(III) occupy the tetrahedral and octahedral

sites, respectively. The most stable phase of Mn_3O_4 is a truncated tetragonal bipyramidal structure in which the (101) facets are primarily exposed with a small percentage of (001) and (100) facets. Growth of the (101) plane depends on the availability of Mn(III), which is formed from the oxidation of Mn(II), because of the greater density of Mn(III) in the (101) plane than that of the (001) plane.

The hybrid of Co_3O_4 nanocrystals coupled with CNTs can cycle over 9000 cycles in 1 M KOH aqueous solution. [132] When assembled into an asymmetric supercapacitor by using activated carbon as the negative electrode, the hybrid capacitor shows excellent cycling performance between 0 and 1.8 V with energy density of 31 Wh kg^{-1} and power density of 3 kW kg^{-1}. Co_3O_4 nanomesh shows a capacitance of 297 F g^{-1} when scanned at 2 A g^{-1} in 3 M KOH aqueous solution though the voltage window is only in the range from 0.25 to 0.5 V (vs. Ag/AgCl),[133] and 288 F g^{-1} could be achieved even at 10 A g^{-1}. However, Co_3O_4 nanostructures with dominant (111) or (100) crystal planes do not have highly expected capacitive performance, and their specific capacitances are below 20 F g^{-1} and degrade rapidly upon increasing in the scan rates. Actually, the dominant (112) crystal plane in the Co_3O_4 nanomesh has much higher surface energy than the conventional (111) and (100) crystal planes, leading to higher activity in supercapacitors. [133] Ni/NiO composite electrode with exposed high surface energy facets exhibits a specific capacitance as high as 2100 F g^{-1}.[134] When assembled as an asymmetric supercapacitor with mesoporous carbon as the negative electrode, the energy and power densities are calculated to be 17 Wh kg^{-1} and 3.5 kW kg^{-1}, respectively. Besides, this asymmetric supercapacitor also delivers good cycling performance over 2000 cycles, which is attributed to that mesoporous wire-like network structure can uniformly distribute the stress across the electrode.

The areal capacitance of the MnO_2 nanowires electrode can be 150 mF cm^{-2} at a current density of 1 mA cm^{-2}. [135] The specific capacitance corresponds to 197.4 F g^{-1} at an equivalent current density of 1.3 A g^{-1}. A solid-state flexible asymmetric supercapacitor was assembled with MnO_2 nanowires and Fe_2O_3 nanotube as the electrodes using a gel electrolyte. It demonstrates excellent stability in a large potential window of 1.6 V and exhibits excellent energy density of 0.55 mWh cm^{-3}. The Mn_3O_4 octahedral nanoparticles show a high capacitance of 260 F g^{-1} at a scan rate of 1 mV s^{-1}. [136] Based on density functional theory calculations, Na preferentially binds to the (101) surface with a binding energy of 2.04 eV, compared to a that of 1.4 eV on the (001) surface.

7 Conclusion and outlook

Over the several years, the increasingly large amount of efforts devoted to electrode materials with tailored facets have resulted in a rich database for their synthesis, characterization and wide applications. This review has summarized recent advances on the synthesis chemistries and distinctive electrochemical properties of electrode materials with tailored facets for Li-ion batteries, aqueous rechargeable lithium batteries, Na-ion batteries, Li-O_2 batteries as well as supercapacitors. The relationship between the crystal facets and their electrochemical activities have been analyzed and discussed.

Generally, the synthesis can be achieved by wet-chemistry route with addition of surfactant. More specifically, through preferential binding of the surfactants with certain crystal planes, the shape of the crystals can be finely tuned. A surfactant is the most important preparation parameter as a morphology-directing agent (or template, or capping agent) in the formation of the desired electrode materials with tailored facets. Besides, the exposure of crystal facets can be controlled to some extent by selecting the appropriate precursor such as the crystal structure and ratio of precursors, and other reaction conditions such as temperature. The precursors can control both the chemical compositions and morphologies of the crystals while temperature can significantly control the speed of crystal growth in some case.

On the other hand, the relationship between the crystal facets and their electrochemical activities can be summarized as follow:

(1) The charge transfer resistance and chemical diffusion coefficient are high along some facets, and exposing these facets can result in a lower energy barrier for faster transport of active ions across the surface of crystals such as TiO_2 as the negative electrode for Li-ion battery. [40, 41]

(2) Some facets have relatively high surface energy and these crystal facets provide reactive sites for fast redox reaction during the charge and discharge process, such as transition metal oxides based on conversion reaction for Li- ion battery,[28-30, 52, 53] catalyst for Li-O_2 battery,[122-124] and electrode materials for supercapacitor. [136]

(3) Active ions can quickly shuttle back and forth in crystals along some directions while they cannot diffuse in the crystal along other directions because a mass of other atoms obstruct their passage. Thus, those facets, perpendicular to the directions that allow transportation of active ions, render a very short transport length for ions during insertion/extraction, such as most intercalation compounds for Li-ion battery and Na-ion battery. [57, 115]

(4) There are many cracks on the exposed crystal planes and these cracks can favor fast ion transportation, such as $LiCoO_2$ with exposed (001) plane and $LiMn_2O_4$ with exposed (400) planes. [12, 65]

(5) A small amount of non-active ions intercalating into channels of electrode materials will lead to capacity fading. Some exposed facets can effectively alleviate non-active ions co-intercalation into the electrode materials because these facets have fewer and smaller channels which only allow active ion intercalate into the material such as LiV_3O_{18} with exposed (100) plane for aqueous rechargeable lithium batteries. [105]

(6) There will be a water molecule chemisorbed near some sites of some facets. This water molecule strengthens the active ions binding on surface sites and increases the binding energy, which lowers the energy barrier for active ion diffusion from the subsurface to this facet, such as $LiFePO_4$ with exposed (010) plane for aqueous rechargeable lithium batteries. [13]

(7) Some ions in the crystals are less densely arranged at some facets and are easily be in close contact with the electrolyte, which makes these ions highly reactive with solvents in the electrolyte, such as $LiMn_2O_4$ with exposed (111) plane for Li-ion battery.[73]

The mechanism for the enhancement of electrochemical performances varies with materials and applications. In case of most electrode materials for batteries, some planes possess relatively low migration energy for active-ions like Li^+ and Na^+ are needed. To predict the electrochemical properties, the active-ion transport way in some complex structures should be confirmed at first. Thus some well-established atomic modeling techniques are of utmost significance for electrode materials optimization. The arrangement of surface atoms and surface energy also mean a lot especially for those electrode materials used in Li-O_2 batteries and supercapacitors. For example, the surface energy for the some planes of electrode materials can be calculated with the help of the Vienna ab initio simulation package (VASP).[19] Currently, despite these significant advances have been achieved in this field, researches on electrode materials with exposed tailored facets are still in preliminary stages. Great opportunities and huge challenges coexist in this field. Throughout this review, we hope to generate more interest in them and boost extensive investigation in related areas. Thus, new vital interests and some challenges listed below are expected to motivate future studies.

To begin with, the technology for the synthesis of electrode materials with tailored facets is facing a challenge in establishing some theories that enable us to predict the type of surface or plane produced by a certain method. In fact, the selection of surfactant still remains empirical currently. Even with the use of same adsorbant as the surface controller, it is possible to prepare nanocrystals of different morphologies. Therefore, the surface binding structures of molecular adsorbants need to be well characterized at the molecular level. Besides, most synthesis strategies involve the use of morphology-controlling agents that must eventually be removed in order to obtain clean facets. This process might lead to some uncontrollable changes to the surface atomic structure of the crystal.

In addition, the integration of several instruments based on *in situ* characterization techniques is necessary. Obviously, *in situ* observations are essential to acquire a true understanding of the electrode surfaces in actions. For example, *in situ* X-ray diffraction [137] and *in situ* TEM techniques [138] are strongly recommended to investigate the mechanism and structural evaluation of electrode materials.

Last but not the least, developing new materials and structures is always expected, especially for Na-ion battery and Li-O_2 batteries. Exploring reliable electrode materials with suitable structures that can allow the intercalation/ deintercalation of Na ions with high efficiency and meanwhile possessing excellent cycling stability is needed for the further development of Na-ion batteries. Designing different structured and efficient catalysts towards both oxygen reduction and/or evolution reactions is one of key research to improve Li – O_2 battery performance. Meanwhile, many new electrochemical energy storage devices emerged in recent years, including Mg-ion battery,[139] Al-ion battery,[140] Zn-ion battery,[141] F- and Cl-ion batteries,[142,143] Na- and K-O_2 battery, [144,145] Li-CO_2 battery, [146] Li-Br_2 battery, [147] metal ion capacitor [148] and so on. However, there are few reports on their electrode materials with tailored facets. Therefore, seeking for new electrode material with tailored facets will be becoming another hot spot in these new electrochemical energy storage devices.

Acknowledgements

Financial support from the Distinguished Young Scientists Program of the National Natural Science Foundation of China (NSFC51425301) is gratefully appreciated.

Notes and references

1 H. G. Yang, C. H. Sun, S. Z. Qiao, J. Zou, G. Liu, S. C. Smith, H. M. Cheng and G. Q. Lu, *Nature*, 2008 , **453**, 638–641.
2 E. M. Larsson, C. Langhammer, I. Zoric and B. Kasemo, *Science*, 2009, **326**, 1091–1094.
3 Y. G. Sun and Y. N. Xia, *Science*, 2002, **298**, 2176–2179.
4 C. L. Pang, R. Lindsay and G. Thornton, *Chem. Soc. Rev.*, 2008 , **37**, 2328–2353.
5 G. Liu, H. G. Yang, J. Pan, Y. Q. Yang, G. Q. Lu and H. M. Cheng, *Chem. Rev.*, 2014, **114**, 9559–9612.
6 M. Chen, B. Wu, J. Yang and N. Zheng, *Adv. Mater.*, 2012, **24**, 862–879.
7 S. Liu, J. Yu and M. Jaroniec, *J. Am. Chem. Soc.*, 2010 , **132**, 11914–11916.
8 L. Zhang, W. Niu and G. Xu, *Nano Today*, 2012, **7**, 586–605.
9 A. Vittadini, A. Selloni, F. P. Rotzinger and M. Gratzel, *Phys. Rev. Lett.*, 1998 , **81** , 2954–2957.
10 D. Larcher and J. M. Tarascon,*Nat. Chem*., 2015, **7**, 19–29.
11 M. R. Lukatskaya, O. Mashtalir, C. E. Ren, Y. D. Agnese, P. Rozier, P. L. Taberna, M. Naguib, P. Simon, M. W. Barsoum and Y. Gogotsi, *Science*, 2013, **341**, 1502–1505.
12 W. Tang, Y. Y. Hou, F. X. Wang, L. L.Liu, Y. P. Wu and K. Zhu, *Nano Lett.*, 2013, **13**, 2036–2040.
13 J. X. Zheng, Y. Y. Hou, Y. D. Duan, X. H. Song, Y. Wei, T. C.Liu, J. T. Hu, H. Guo, Z. Q. Zhuo, L. L. Liu, Z. L. Chang, X. W. Wang, D. Zherebetskyy, Y. Fang, Y. Lin, K. Xu, L. W. Wang, Y. P. Wu and F. Pan, *Nano Lett*., 2015, **15**, 6102–6109.
14 Y. Shi, S. L. Chou, J. Z. Wang, D. Wexler, H. J. Li, H. K. Liu and Y. P. Wu, *J. Mater. Chem.*, 2012, **22**, 16465 – 16470.
15 Y. Shi, J. Z. Wang, S. L. Chou,D. Wexler, H. J. Li, K. Ozawa, H. K. Liu and Y. P. Wu, *Nano Lett.*, 2013, **13**, 4715–4720.
16 Y. Shi, J. Gao, H. D. Abruna, H. J. Li, H. K. Liu, D. Wexler, J. Z. Wang and Y. P. Wu, *Chem. Eur. J.*, 2014, **20** , 5608–5612.
17 W. Q. Fang, X. Q. Gong and H. G. Yang, *J. Phys. Chem. Lett.*, 2011, **2**, 725–734.
18 W. J. Ong, L. L. Tan, S.P. Chai, S. T. Yong and A. R. Mohamed, *Nanoscale*, 2014, **6**, 1946–2008.
19 H. Sun, H. M. Ang, M. O. Tade and S. Wang, J. Mater. Chem. A , 2013, **1**, 14427–14442.
20 G. L. Xu, Q. Wang, J. C. Fang, Y. F. Xu, J. T. Li, L. Huang and S. G. Sun, *J. Mater. Chem. A*, 2014, **2**, 19941–19962.
21 J. B. Goodenough and K. S. Park, *J. Am. Chem. Soc.*, 2013, **135**, 1167–1176.
22 T. Stephenson, Z. Li, B. Olsen and D. Mitlin, *Energy Environ. Sci.*, 2014, **7**, 209–231.
23 Y. P. Wu, E. Rahm and R. Holze, *Electrochim. Acta*, 2002, **47**, 3491–3507.

24 C. Li, H. P. Zhang, L. J. Fu, H. Liu, Y. P. Wu, E. Rahm, R. Holze and H. Q. Wu, *Electrochim. Acta*, 2006, **51**, 3872–3883.
25 J. S. Chen, Y. L. Tan, C. M. Li, Y. L. Cheah, D. Luan, S. Madhavi, F. Y. C. Boey, L. A. Archer and X. W. Lou, *J. Am. Chem. Soc.*, 2010 , **132**, 6124–6130.
26 Y. M. Jiang, K. X. Wang, X. Y. Wu, H. J. Zhang, B. M. Bartlett and J. S. Chen, *ACS Appl. Mater. Interfaces*, 2014, **6**, 19791-19796.
27 X. Wang, X. Cao, L. Bourgeois, H. Guan, S. Chen , Y. Zhong, D. M. Tang, H. Li, T. Zhai, L. Li, Y. Bando and D. Golberg, *Adv. Funct. Mater.*, 2012, **22**, 2682–2690.
28 D. Su, M. Ford and G. Wang, *Sci. Rep.*, 2012, **2**, 924–930.
29 D. Su, X. Xie, S. Dou and G. Wang, *Sci. Rep.*, 2014, **4**, 5753–5761.
30 X. Xiao, X. Liu, H. Zhao, D. Chen, F. Liu, J. Xiang, Z. Hu and Y. Li. *Adv. Mater.*, 2012, **24**, 5762–5766.
31 L. J. Fu, H. Liu, H. P. Zhang, C. Li, T. Zhang, Y. P. Wu, R. Holze and H. Q. Wu, *Electrochem. Commun.*, 2006, **8**, 1–4.
32 L. J. Fu, T. Zhang, Q. Cao, H. P. Zhang and Y. P. Wu. *Electrochem. Commun.*, 2007, **9**, 2140–2144.
33 C. Wang, F. Wang, Y. Zhao, Y. Li, Q. Yue, Y. Liu, Y. Liu, A. A. Elzatahry, A. Al-Enizi, Y. Wu, Y. Deng and D. Zhao, *Nano Res.*, 2016, DOI: 10.1007/s12274-015-0976-7.
34 L. Liu, Q. Fan, C. Sun, X. Gu, H. Li, F. Gao, Y. Chen and L. Dong, *J. Power Sources*, 2013, **221**, 141–148.
35 B. Qiu, M. Xing and J. Zhang, *J. Am. Chem. Soc.*, 2014, **136**, 5852–5855 .
36 L. Ren, Y. Liu, X. Qi, K. S. Hui, K. N. Hui, Z. Huang, J. Li, K. Huang and J. Zhong, *J. Mater. Chem.*, 2012, **22**, 21513–21518.
37 S. Liu, H. Jia, L. Han, J. Wang, P. Ga, D. Xu, J. Yang and S. Che, *Adv. Mater.*, 2012, **24**, 3201–3204.
38 J. Liu, J. S. Chen, X. Wei, X. W. Lou and X. W. Liu, *Adv. Mater.*, 2011, **23**, 998–1002.
39 S. Ding, J. S. Chen, Z. Wang, Y. L. Cheah, S. Madhavi, X. Hu and X. W. Lou, *J. Mater. Chem*., 2011, **21**, 1677–1680.
40 R. Hengerer, L. Kavan, P. Krtil and M. Gratzel, *J. Electrochem. Soc*., 2000, **147**, 1467–1472.
41 C. H. Sun, X. H. Yang, J. S. Chen, Z. Li, X. W. Lou, C. Li, S. C. Smith, G. Q. Lu and H. G. Yang, *Chem. Commun.*, 2010, **46**, 6129–6131.
42 G. J. Wang, J. Gao, L. J. Fu, N. H. Zhao, Y. P. Wu and T. Takamura, *J. Power Sources*, 2007, **174**, 1109–1112.
43 Y. Shi, J. Gao, H. D. Abruña, H. K. Liu, H. J. Li, J. Z. Wang and Y. P. Wu, *Nano Energy*, 2014, **8**, 297 – 304.
44 T. Zhang, H. P. Zhang, L. C. Yang, B. Wang, Y. P. Wu and T. Takamura, *Electrochim. Acta*, 2008, **53**, 5660–5664.
45 T. Zhang, L. Fu, J. Gao, L. Yang, Y. Wu and H. Wu, *Pure Appl. Chem.*, 2006, **78**, 1889–1896.
46 T. Zhang, J. Gao, L. J. Fu, L. C. Yang, Y. P. Wu and H. Q. Wu, *J. Mater. Chem.*, 2007, **17**, 1321–1325.
47 S. C. Jung and Y. K. Han, *Phys. Chem. Chem. Phys.*, 2011, **13**, 21282–21287.
48 S. W. Lee, M. T. McDowell, J. W. Choi and Y. Cui, *Nano Lett.*, 2011, **11**, 3034–3039.
49 N. Zhao, G. Wang, Y. Huang, B. Wang, B. Yao and Y. Wu, *Chem. Mater.*, 2008, **20**, 2612–2614.
50 N. H. Zhao, L. C. Yang, P. Zhang, G. J. Wang, B. Wang, B. D. Yao and Y. P. Wu, *Mater. Lett.*, 2010, **64**, 972 – 975.
51 C. Wang, G. Du, K. Stahl, H. Huang, Y. Zhong and J. Z. Jiang, *J. Phys. Chem. C*, 2012, **116**, 4000 – 4011.
52 J. Zhu, Z. Yin, D. Yang, T. Sun, H. Yu, H. E. Hoster, H. H. Hng, H. Zhang and Q. Yan, *Energy Environ. Sci*., 2013, **6** , 987–993.
53 X. Duan, L. Mei, J. Ma, Q.Li, T. Wang and W. Zheng, *Chem. Commun.*, 2012, **48**, 12204–12206.
54 W. Li, Y. X. Yin, S. Xin, W. G. Song and Y. G. Guo, *Energy Environ. Sci.*, 2012, **5**, 8007–8013.
55 H. Li, X. Liu, T. Zhai, D. Li and H. Zhou, *Adv. Energy Mater.*, 2013, **3**, 428–432.
56 Y. P. Wu, E. Rahm and R. Holze, *J. Power Sources*, 2003, **114**, 228–236.
57 H. T. Xu, H.Zhang, L. Liu, Y. Feng and Y. Wang, *ACS Appl. Mater. Interfaces*, 2015, DOI: 10.1021/acsami.5b06844.
58 W. Sun, F. Cao, Y. Liu, X. Zhao, X. Liu and J. Yuan, *J. Mater. Chem.*, 2012, **22**, 20952–20957.
59 F. Fu, G. L. Xu, Q. Wang, Y. P. Deng, X. Li, J. T. Li, L. Huang and S. G. Sun, *J. Mater. Chem. A*, 2013, **1**, 3860 – 3864.
60 L. Wang, X. He, W. Sun, J. Wang, Y. Li and S. Fan, *Nano Lett.*, 2012, **12**, 5632–5636.
61 L. Chen, Y. Su, S. Chen, N. Li, L. Bao, W. Li, Z. Wang, M. Wang and F. Wu, Adv. Mater., 2014, 26, 6756–6760.
62 X. L. Pan, C. Y. Xu and L. Zhen, *CrystEngComm.*, 2012, **14**, 6412–6418.
63 X. Wang, Q. Qu, Y. Hou, F. Wang and Y. Wu, *Chem. Commun.*, 2013, **49**, 6179–6181.
64 Q. Cao, H. P. Zhang, G. J. Wang, Q. Xia, Y. P. Wu, H. Q. Wu, *Electrochem. Commun.*, 2007, **9**, 1228–1232.
65 X. Xiao, X. Liu, L. Wang, H. Zhao, Z. Hu, X. He and Y. Li, *Nano Res*., 2012, **5**, 395–401.
66 F. X. Wang, S. Y. Xiao, Y. Shi, L. L. Liu, Y. S. Zhu, Y. P. Wu, J. Z. Wang, R. Holze, *Electrochim. Acta*, 2013, **93**, 301–306.
67 Y. Liu, B. Zhang, F. Wang, Z. Wen and Y. Wu, *Pure Appl. Chem.*, 2014, **86**, 593–609.
68 F. X. Wang, S. Y. Xiao, X. W. Gao, Y. S. Zhu, H. P. Zhang, Y. P. Wu and R. Holze, *J. Power Sources*, 2013, **242**, 560–565.
69 M. Hirayama, H. Ido, K. S. Kim, W. Cho, K. Tamura, J. Mizuki and R. Kanno, *J. Am. Chem. Soc.*, 2010 , **132**, 15268–15276.
70 Y. L. Ding, J. Xie, G. S. Cao, T. J. Zhu, H. M. Yu and X. B. Zhao, *Adv. Funct. Mater.*, 2011, **21**, 348–355.
71 D. K. Kim,P. Muralidharan, H. W. Lee, R. Ruffo, Y. Yang, C. K. Chan, H. Peng, R. A. Huggin and Y. Cui, *Nano Lett.*, 2008, **8**, 3948–3952.
72 H. W. Lee, P. Muralidharan, R. Ruffo, C. M. Mari, Y. Cui and D. K. Kim, *Nano Lett.*, 2010, **10**, 3852–3856.
73 J. S. Kim, K. S. Kim, W. Cho, W. H. Shin, R. Kanno and J. W. Choi, *Nano Lett.*, 2012, **12**, 6358–6365.
74 H. Kawaura, D. Takamatsu, S. Mori, Y. Orikasa, H. Sugaya, H. Murayama, K. Nakanishi, H. Tanida, Y. Koyama, H. Arai, Y. Uchimoto and Z. Ogumi, *J. Power Sources*, 2014, **245**, 816–821.
75 J. Rana, S. Glatthaar, H. Gesswein, N. Sharma, J. R. Binder, R. Chernikov, G. Schumacher and J. Banhart, *J. Power Sources*, 2014, **255**, 439–449.
76 K. R. Chemelewski, E. S. Lee, W. Li and A. Manthiram, *Chem. Mater.*, 2013, **25**, 2890–2897.
77 F. Wang, S. Xiao, Z. Chang, Y. Yang and Y. Wu, *Chem. Commun.*, 2013, **49**, 9209– 9211.
78 F. Wang, Y. Liu, X. Wang, Z. Chang, Y. Wu and R. Holze, *ChemElectroChem*, 2015, **2**, 1024–1030.
79 J. Li, R. Yao and C. Cao, *ACS Appl. Mater. Interfaces*, 2014, **6**, 5075– 5082.
80 Y. Wu, C. Cao, Y. Zhu,J. Li and L. Wang, *J. Mater. Chem. A*, 2015, **3**, 1 5523–15528.
81 H. Liu, C. Li, H. P. Zhang, L. J. Fu, Y. P. Wu and H. Q. Wu, *J. Power Sources*, 2006, **159**, 717–720.
82 H. Liu, P. Zhang, G. C. Li, Q. Wu and Y. P. Wu, *J. Solid State Electrochem.*, 2008, **12**, 1011–1015.
83 S. Xiao, F. Wang, Y. Yang, Z. Chang and Y. Wu, *RSC Adv.*, 2014, **4**, 76–81.
84 S. Y. Xiao, Y. Q. Yang, M. X. Li, F. X. Wang, Z. Chang, Y. P. Wu and X. Liu, *J. Power Sources*, 2014, **270**, 53–58.
85 Y. S. Zhu, S. Y. Xiao, M. X. Li, Z. Chang, F. X. Wang, J. Gao and Y. P. Wu, *J. Power Sources*, 2015, **288**, 368–375.
86 D. Morgan, A. V. Ven and G. Ceder, *Electrochem. Solid-State Lett.*, 2004, **7**, A30–A32.
87 C. Nan, J. Lu, C. Chen, Q. Peng and Y. Li, *J. Mater. Chem.*, 2011, **21**, 9994–9996.

88 B. Pei, H. Yao, W. Zhang and Z. Yang, *J. Power Sources*, 2012, **220**, 317–323.
89 Y. Liu, J. Gu, J. Zhang , F. Yu, J. Wang, N. Nie and W. Li, *RSC Adv.*, 2015, **5**, 9745–9751.
90 R. Mei, X. Song, Y. Yang, Z. An and J. Zhang, *RSC Adv.*, 2014, 4,5746–5752.
91 F. Wang, S. Xiao, M. Li, X. Wang, Y. Zhu, Y. Wu, A. Shirakawa, J. Peng, *J. Power Sources*, 2015, **287**, 416–421.
92 F. X. Wang, S. Y. Xiao, Z. Chang, M. X. Li, Y. P. Wu, R. Holze, *Int. J. Electrochem. Sci.*, 2014, **9**, 6182–6190.
93 H. J. Yu and H. S. Zhou, *J. Phys. Chem. Lett.*, 2013, **4**, 1268−1280.
94 F. Wang, Z. Chang, X. Wang, Y. Wang, B. Chen, Y. Zhu and Y. Wu, *J. Mater. Chem. A*, 2015, **3**, 4840–4845.
95 G. Z. Wei, X. Lu, F. S. Ke, L. Huang, J. T. Li, Z. X. Wang, Z. Y. Zhou and S. G. Sun, *Adv. Mater.*, 2010, **22**, 4364–4367.
96 C. L. Hu, H. H. Yi, F. X. Wang, S. Y. Xiao, Y. P.Wu, D. Wang and D. L. He, *J. Power Sources*, 2014, **255**, 355–359.
97 W. Chen, M. Lan, D. Zhu, C. Ji, X. Feng, C. Yang, J. Zhang and L. Mi, *J. Mater. Chem. A*, 2013, **1**, 10912–10917.
98 R. J. Gummow and Y.He, *J. Power Sources*, 2014, **253**, 315–331.
99 D. Rangappa, K. D. Murukanahally, T. Tomai, A. Unemoto, and I. Honma, *Nano Lett*., 2012, **12**, 1146− 1151.
100 W. Li, J. R. Dahn and D. S. Wainwright, *Science*, 1994, **264**, 1115–1118.
101 G. Wang, L. Fu, N. Zhao, L. Yang, Y. Wu and H. Wu, *Angew. Chem. Int . Ed.*, 2007, **46**, 295–297.
102 W. Tang, Y. Zhu, Y. Hou, L. Liu, Y. Wu, K. P. Loh, H. Zhan and K. Zhu, *Energy Environ. Sci.*, 2013, **6**, 2093– 2104.
103 Z. Chang, Y. Yang, M. Li, X. Wang and Y. Wu, *J. Mater. Chem. A*, 2014, **2**, 10739–10755.
104 H. Kim, J. Hong, K. Y. Park, H. Kim, S. W. Kim and K. Kang, *Chem. Rev.*, 2014, **114**, 11788−11827.
105 L. Liang, M. Zhou and Y. Xie, *Chem. Asian J.*, 2012, **7**, 565–571.
106 H. Li, T. Zhai, P. He, Y. Wang, E. Hosono and H. Zhou, *J. Mater. Chem*., 2011, **21**, 1780–1787.
107 S. Zhang, Y. Li, C. Wu, F. Zheng and Y. Xie, *J. Phys. Chem. C*, 2009, **113**, 15058–15067.
108 W. Tang, X. W. Gao, Y. S. Zhu, Y. B. Yue, Y. Shi, Y. P. Wu and K. Zhu, *J. Mater. Chem.*, 2012, **22**, 20143– 20145.
109 G. H. Newman and L. P. Klemann, *J. Electrochem. Soc.*, 1980, **127**, 2097–2099.
110 N. Yabuuchi, K. Kubota, M. Dahbi and S. Komaba, *Chem. Rev.*, 2014, **114**, 11636−11682.
111 D. Su, C. Wang, H. Ahn and G. Wang, *Phys. Chem. Chem. Phys*., 2013, **15**, 12543−12550.
112 D. Su, X. Xie and G. Wang, *Chem. Eur. J.*, 2014, **20**, 3192−3197.
113 D. W. Su, S. X. Dou and G. X. Wang, *J. Mater. Chem. A*, 2014, **2**, 11185–l1194.
114 X. Jiang, S. Liu, H. Xu, L. Chen, J. Yang and Y. Qian, *Chem. Commun.*, 2015, **51**, 8480−8483.
115 D. Su, C. Wang, H. J. Ahn and G. Wang, *Chem. Eur. J.*, 2013, **19**, 10884–10889.
116 D. Su, H. J. Ahn and G. Wang, *NPG Asia Mater.*, 2013, **5**, e70.
117 K. M. Abraham and Z. Jiang, *J. Electrochem. Soc.*, 1996, **143**, 1-5.
118 T. Ogasawara, A. D´ebart, M. Holzapfel, P. Novak and P. G. Bruce, *J. Am. Chem. Soc.*, 2006, **128**, 1390–1393.
119 P. G. Bruce, S. A. Freunberger, L. J. Hardwick and J. M. Tarascon, *Nat. Mater.*, 2012, **11**, 19–29.
120 Z. Guo, X. Dong, Y. Wang and Y. Xia, *Chem. Commun.*, 2015, **51**, 676–678.
121 A. C. Luntz and B. D. McCloskey, *Chem. Rev.*, 2014, **114**, 11721−11750.
122 D. Su, S. Dou and G. Wang, NPG Asia Mater., 2015, 7,e155
123 C. J. Johnson, E. Dujardin, S. A. Davis, C. J. Murphy and S. Mann, J. Mater. Chem., 2002, 12, 1765–1770.
124 D. Su, S. Dou and G. Wang, *Sci. Rep.*, 2014, **4**, 5767−5775.
125 F. Wang, S. Xiao, Y. Hou, C. Hu, L. Liu and Y. Wu, *RSC Adv.*, 2013, **3**, 13059–13084.
126 F. Yu, L. Zhu, T. You, F. Wang and Z. Wen, *RSC Adv.*, 2015, **5**, 96165–96169.
127 X. Liu, Y. Zhang, T. Wu and J. Huang, *Chem. Commun*., 2012, **48**, 9992–9994.
128 R. Li, X. Ren, F. Zhang, C. Du and J. Liu, *Chem. Commun*., 2012, **48**, 5010–5012.
129 W. Tang, L. Liu, S. Tian, L. Li, Y. Yue, Y. Wu and K. Zhu, *Chem. Commun.*, 2011, **47**, 10058–10060.
130 Q. Qu, Y. Zhu, X. Gao and Y. Wu, *Adv. Energy Mater.*, 2012, **2**, 950–955.
131 X. Wang, M. Li, Z. Chang, Y. Yang, Y. Wu and X. Liu, *ACS Appl. Mater. Interfaces*, 2015, **7**, 2280−2285.
132 X. Wang, M. Li, Z. Chang, Y. Wang, B. Chen, L. Zhang and Y. Wu, *J. Electrochem. Soc.*, 2015, **162**, A1966−A1971.
133 Y. Wang, H. J. Zhang, J. Wei, C. C. Wong, J. Lin and A. Borgna, *Energy Environ. Sci.*, 2011, **4**, 1845–1854.
134 A. Paravannoor, T. S. Sonia, S. V. Nair and A. Balakrishnan, *Mater. Lett.*, 2014, **135**, 180 – 183.
135 P. Yang, Y. Ding, Z. Lin, Z. Chen, Y. Li, P. Qiang, M. Ebrahimi, W. Mai, C. P. Wong and Z. L. Wang, *Nano Lett.*, 2014, **14**, 731−736.
136 M. P. Yeager, W. Du, Q. Wang, N. A. Deskins, M. Sullivan, B. Bishop, D. Su, W. Xu, S. D. Senanayake, R. Si, J. Hanson and X. Teng, *ChemSusChem*, 2013, **6**, 1983 – 1992.
137 S. Misra, N. Liu, J. Nelson, S. S. Hong, Y. Cui and M. F. Toney, *ACS Nano*, 2012, **6**, 5465–5473.
138 J. Y. Huang, L. Zhong, C. M. Wang, J. P. Sullivan, W. Xu, L. Q. Zhang, S.X. Mao, N. S. Hudak, X. H. Liu, A. Subramanian, H. Fan, L. Qi, A. Kushima, J. Li, *Science*, 2010, **330**, 1515–1520.
139 J. Muldoon, C. B. Bucur and T. Gregory, *Chem. Rev.*, 2014, **114**, 11683−11720.
140 F. Wang, F. Yu, X. Wang, Z. Chang, L. Fu, Y. Zhu, Z. Wen, Y. Wu and W. Huang, *ACS Appl. Mater. Interfaces*, 2016, DOI: 10.1021/acsami.5b06142.
141 C. Xu, B. Li, H. Du and F. Kang, *Angew. Chem. Int. Ed.*, 2012 , **51**, 933–935.
142 X. Zhao, S. Ren, M. Bruns, M. Fichtner, *J. Power Sources*, 2014, **245**, 706–711.
143 X. Zhao, Z. Z. Karger, D.Wang and M. Fichtner, *Angew. Chem. Int. Ed.*, 2013 , **52**, 13621–13624.
144 P. Hartmann, C. L. Bender, M. Vracar, A. K. Dürr, A. Garsuch, J. Janek and P. Adelhelm, *Nature Mater.*, 2013, **12**, 228–232 .
145 X. Ren and Y. Wu, *J. Am. Chem. Soc.*, 2013, **135**, 2923−2926.
146 Y. Liu, R. Wang , Y. Lyu, H. Li and L. Chen, *Energy Environ. Sci*., 2014, **7**, 677–681.
147 Z. Chang, X. Wang, Y. Yang, J. Gao, M. Li, L. Liu and Y. Wu, *J. Mater. Chem. A*, 2014, **2**, 19444–19450.
148 F. Wang, X. Wang, Z. Chang, X. Wu, X. Liu, L. Fu, Y. Zhu, Y. Wu and W. Huang, *Adv. Mater.*, 2015, **27**, 6962–6968.

Table of content:

Electrode materials with tailored facets for electrochemical energy storage

Faxing Wang, Xiaowei Wang, Zheng Chang, Yusong Zhu, Lijun Fu, Xiang Liu, and Yuping Wu

This review highlights electrode materials with predominantly exposed facets facilitating better electrochemical performances in electrochemical energy storage applications.